Clemson University
TigerPrints

All Theses | Theses

8-2013

Particle Electrophoresis and Magnetophoresis in Microchannels

Litao Liang
Clemson University, lliang@clemson.edu

Follow this and additional works at: https://tigerprints.clemson.edu/all_theses

 Part of the Mechanical Engineering Commons

Recommended Citation
Liang, Litao, "Particle Electrophoresis and Magnetophoresis in Microchannels" (2013). *All Theses*. 1699.
https://tigerprints.clemson.edu/all_theses/1699

This Thesis is brought to you for free and open access by the Theses at TigerPrints. It has been accepted for inclusion in All Theses by an authorized administrator of TigerPrints. For more information, please contact kokeefe@clemson.edu.

PARTICLE ELECTROPHORESIS AND MAGNETOPHORESIS IN MICROCHANNELS

A Thesis
Presented to
the Graduate School of
Clemson University

In Partial Fulfillment
of the Requirements for the Degree
Master of Science
Mechanical Engineering

---

by
Litao Liang
August 2013

Accepted by:
Dr. Xiangchun Xuan, Committee Chair
Dr. Rui Qiao
Dr. John R. Saylor
Dr. Richard Figliola

ABSTRACT

In current pharmaceutical and biotechnology industries with clinical applications, an increased demand for flow control and cell manipulation on the micrometer scale has emerged. Electrokinetic, magnetic and many other physics fields have been exploited to meet this demand. However, due to the requirement for sophisticated micro-structures and the interference of the increasing significance of many 'trivial' physics properties (surface potential, permittivity, etc.) at the smaller scale, most applications encounter poor maneuverability and high operation/fabrication complexity issues. Very few attempts have been made to bypass these requirements while maintaining the same control and efficiency. This thesis research investigates the fundamental behaviors in microfluidic particle transportation. Then, with a thorough comprehension of the governing parameters and key effects, practical applications can be designed and developed to resolve the aforementioned microfluidic technique issues of electrophoresis and magnetophoresis.

This thesis consists of two main parts. In the first section, the basic manipulation principle and subsequent applications in particle electrophoresis are discussed. Based on an observed wall-induced particle deflection in a straight microchannel, this thesis developed a method to three-dimensionally focus particle stream to the microchannel center. This application only relied on the particle confinement with respect to the microchannel; no particular external forces had to be exerted since this phenomenon was self-developing along with the traveling in the lengthwise direction.

The second half of this work shifted the focus to particle magnetophoresis in a straight microchannel. An analytical model was built that solved the coupled magnetic and flow field, confirmed the experimental observations and enabled predictions for other plausible applications.

Following that, this work utilized this *negative* magnetophoretic deflection to implement a diamagnetic particle focusing in a T-shaped microchannel. Particle ferrofluid flow and axillary sheath flow moved within each half of the microchannel and, the magnetophoretic deflection took effect inside the ferrofluid half where the particles were focused on the interface between the two halves. This arrangement required only one magnet with the help of the sheath flow to restrain the effective magnetophoretic deflection, which tremendously reduced the fabrication complexity and extended the channel-magnet distance to a smaller magnitude, therefore enhanced the throughput.

Lastly, the same T-shaped microchannel was proved to perform high efficient particle separation. In addition to the *negative* magnetophoresis induced deflection for the diamagnetic particle was applied, the ‘attraction’ for the magnetic particle was present at the same time due to the *opposite* reaction: positive magnetophoresis. Initially mixed diamagnetic and magnetic particle sample were injected into the microchannel and, the opposite responses to the magnetic field formed a continuous separation of these two types at the end of the microchannel. Compared to the batch-mode MACS (magnetic cell sorter), this method undoubtedly made an improvement in both the throughput and operative difficulties.

Both the electrophoretic and magnetophoretic applications were composed of straight microchannels or sections with rectangular sections, which are the simplest and the most typical structures in microfluidic devices. This tremendously reduced the fabrication cost and complexity, while maintaining the same effectiveness and efficiency in particle controls of the conventional methods, which also increase the feasibility of massive production. In particular, the magnetophoretic applications helped to avoid the magnets arrangement and low processing speed issues, and therefore provided a simple but effective method for flow cytometry application.

ACKNOWLEDGEMENTS

First of all, I would like to thank my advisor, Dr. Xiangchun Xuan, for giving me the opportunities to learn and experiment on microfluidic research and study. Dr. Xuan gave me much help and advices on many aspects of microfluidic research, and I feel appreciated for Dr. Xuan's efforts to letting me join and attend some major fluid science conferences. I've learnt a lot from Dr. Xuan through my past graduate research and life with him.

Next, I would also like to thank all my co-workers and teammates: Junjie Zhu, Christopher Church, Sriram Sridharan, Bhaskar Ramesh, Srijeet Sathyamurth, Saurin Patel, Remy Zeng and Chen Chen. They gave me strong support in conducting experiments and simulation, as well as their generous help throughout each one of my projects.

Meanwhile, I would like to thank the National Science Foundation, NSF for funding my research for last few years.

At last, I would like to thank my parents and grandparents for their love and encourage during my stay in Clemson, as they were far away in China and still gave me strong mental support.

TABLE OF CONTENTS

Page

Table of Contents (Continued)

Page

Table of Contents (Continued)

Page

Table of Contents (Continued)

Page

LIST OF FIGURES

Figure Page

List of Figures (Continued)

Figure Page

List of Figures (Continued)

Figure Page

List of Figures (Continued)

Figure Page

List of Figures (Continued)

Figure Page

NOMENCLATURE

a	particle diameter
B_s	residual magnetic flux density
d	average diameter of the magnetic nanoparticles
E	electric field strength
ε_f	permittivity of the fluid medium
$\mathbf{F}_\mathrm{m}$	magnetic “buoyancy” force
$\mathbf{F}_w$	wall-induced repulsive force
f_{CM}	Clausius–Mossotti (CM) factor
f_D	drag coefficient accounting for the particle-wall interactions
$\mathbf{H}$	magnetic field
$\mathbf{H}_{demag}$	particle’s self-demagnetization magnetic field
$\mathbf{H}_{in}$	effective magnetic field inside particle
k_B	Boltzmann constant
$\mathbf{M}$	magnetization
$\mathbf{M}_f$	effective magnetization of the ferrofluid
$\mathbf{M}_p$	effective magnetization of the particle
M_r	remanent magnetization of the magnet
M_s	residual magnetization of the permanent magnet
M_d	saturation moment of the magnetic nanoparticles
M_{sat}	saturation magnetization of the ferrofluid
Q	flow rate

$\mathbf{r}_p$ instantaneous position of the center of a particle

$\mathbf{r}_0$ initial position of the particle center

T temperature

t time

$\mathbf{U}_p$ particle velocity

$\mathbf{U}_m$ magnetophoretic particle velocity

$\mathbf{U}_{EK}$ electrokinetic particle velocity

$\mathbf{U}_w$ wall-induced particle velocity

U_f flow velocity

U_{ep} electrophoretic velocity

μ_0 permeability of free space

μ_m dynamic viscosity of the solution medium

μ_{Ek} electrokinetic particle mobility

V_p volume of the particle

w_p half of the particle stream width

χ susceptibility

ς_p surface charge of the particle

ϕ volume fraction of magnetic nanoparticles

δ smallest particle center to wall separation distance

η kinetic viscosity of ferrofluids

CHAPTER 1 : INTRODUCTION

1.1. Aims and Motivation

With the emergence of microfluidics in the early 1980s, in response to the progressively revolutionizing molecular biotechnology and clinical pathology disciplines, more effort was made to conduct research on and employ miniaturized devices that capture and control fluids at the sub-millimeter scale. For example, in the pharmaceutical industry, researchers needed to find an effective way to increase the bioavailability and stability for targeted drug delivery of medical particles of micrometer or even submicron sizes. In the energy field, people can create effective fuel cells and biofuels with the knowledge of microfluidics, specifically, they can capture and concentrate typical photovoltaic cells to generate electricity from solar energy absorbed by these cells.

Microfluidics studies the fluids that are constrained to small volumes or require low energy input. The use of these size-reduced chips to conduct biomedical research and create clinically useful technologies has a number of significant advantages. First, miniaturized size means low fluid volume consumption and faster processing speed, which becomes critical when working with expensive or scarce reagents. Second, the proven micro-fabrication technique greatly reduces the fabrication costs and raises the feasibility for mass production. Third and last, these highly-integrated chip-sized devices make portable multifunctional clinical services possible.

To date, numerous applications have been developed with the thriving microfluidic technology. These technologies include inkjet printheads, DNA chips, lab-on-a-chip (LOC) technology, etc. Varieties of force fields have been demonstrated to

implement particle manipulations (e.g., focusing [1], trapping, concentration [2], separation and sorting [3], [4]) in microfluidic devices, among which electric [5], [6], acoustic [7], [8], magnetic [9], [10], and optical [11], [12] forces are most often employed. Practical applications include the detection of hybridized DNA molecules [13], separation of human breast cancer cells from blood [14] and trapping of single HeLa cells [15].

However, in most microfluidic devices, the control principle always relies on the field gradients inside the microchannels, such as the electric field gradients. Such field gradients are generated by either embedded electrode arrays or curved, constricting, and expanding microchannel geometries. Both methods require precise fabrication and sufficient chip space, which significantly limit the feasibility of integration with other functional sections onto a single chip. It is clear that current microfluidic designs and controls need to be optimized towards simplicity and reduced size in order to attain the original goal of being miniature, compact and cost-effective. Therefore, in this work the first goal was to investigate the fundamentals of these microfluidic motions, including the force origins, manipulation principles and the theoretical evaluation. Based on that, the next goal was to develop effective particle manipulation applications that could realize advanced particle controls with high precision and efficiency. The established methods were used to resolve the fabrication and operation issues in conventional electrokinetic and magnetic controls.

Typically, polystyrene particles are used as substitutes for biological cells in early research stages, while real cells are used in successful applications. Polypropylene particles are chosen for microfluidic experiment because they are similar to common cells

in size and physical properties (electric conductivity, magnetic susceptibility, etc.). The nature and key parameters regarding electrophoresis and magnetophoresis are presented below.

1.2. Background of Electrokinetic Phenomena

1.2.1. Electrical Double Layer

Most substances will obtain a surface electric charge when placed into or in contact with fluid. In many cases, such surface charges come from ionization of the surface group. If a surface contains acidic groups, their dissociation gives rise to a negatively charged surface. If the liquid is a polar fluid, then the dipole molecules will tend to be oriented in a specific direction at the interface and hence generate a potential difference at the boundary[16]. In the case of microfluidic experiments, the microchannel is fabricated most often with polydimethylsiloxane (PDMS) or other polymer materials, and the micro-particles and cells used in experiments typically possess a dielectric property compared to the electrolyte medium. In this fashion, the channel walls and particle surfaces are instantly negatively charged when subjected to electrolyte medium. The absorbed ions on the object surface form the first layer. These will stably reside on the surface and produce a surface potential of a definite value termed zetal potential (ζ), and it is a material-related property.

On the other hand, the counter-ions in the surrounding medium are attracted by the Coulomb force that generates a second layer to electrically screen the first layer. As the counter-ions are attached loosed to the object surface, they are flushed away and

replaced with new counter-ions if there is relative motion between the object and surrounding medium. More importantly, the counter-ion concentration decays rapidly as the distance to the object surface increases then eventually vanishes to zero in the bulk fluid region.

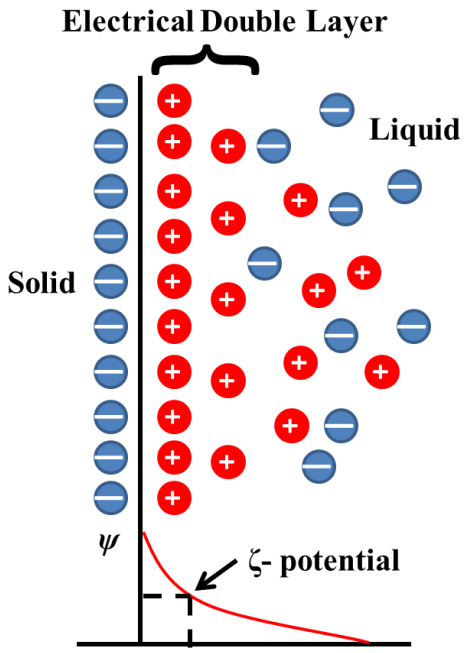

Fig. 1-1: Diagram of the ion distribution and the resulting electric double layer formed near a solid surface.

Together, these two layers create the electrical double layer at the object surface, which is a fundamental phenomenon that guarantees the electrokinetic motions in microfluidics. Theoretically, the potential formed at the interface between these two layers is named as zetal potential, ζ-potential. Usually, this potential has a fixed value determined by the materials of the solid wall and electrolyte medium. The electric

potential ψ decays rapidly from ζ-potential to zero only a few nanometers away from the solid surface.

1.2.2. Electroosmosis

When an electric field E is applied across the system, the excessive counter-ions near the solid surface feel this field source and react towards the cathode terminal; a phenomenon called electroosmosis. The electroosmotic velocity U_{eo} can be expressed as[17]:

$$U_{eo} = -\frac{\varepsilon_f \zeta_w}{\mu_f}\left(1-\frac{\psi}{\zeta_w}\right)E \qquad \text{(Eq. 1-1)}$$

where ε_f and μ_f are the permittivity and viscosity of the fluid medium, ζ_w is the zetal potential on the electrical double layer (EDL) of the microchannel wall, E is the electric field strength, and ψ is the electric potential at certain location within the microchannel.

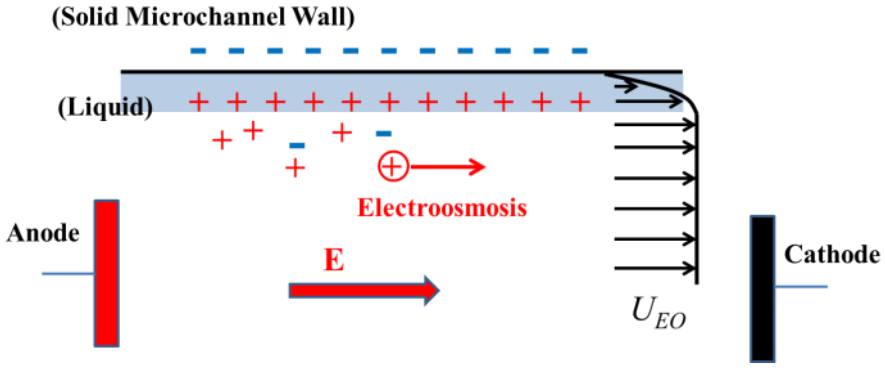

Fig. 1-2: Illustration of the electroosmosis phenomenon close to the microchannel surface.

As the electrical potential ψ drops rapidly to zero with increasing distance to the solid surface, the electrical potential in the bulk fluid region can be deemed as 0, and the electroosmotic velocity U_{eo} in the bulk fluid region remains constant, which reduced to:

$$U_{eo} = -\frac{\varepsilon_f \zeta_w}{\mu_f} E \qquad \text{(Eq. 1-2)}$$

1.2.3. Electrophoresis

For the particle/cell suspended in the electrolyte medium, EDL also forms at its surface area. Likewise, there will also be excessive counter-ions adjacent to the particle/cell surface. When an external electric field E is applied, these counter-ions move with an electroosmotic velocity expressed in Eq. 1-2.

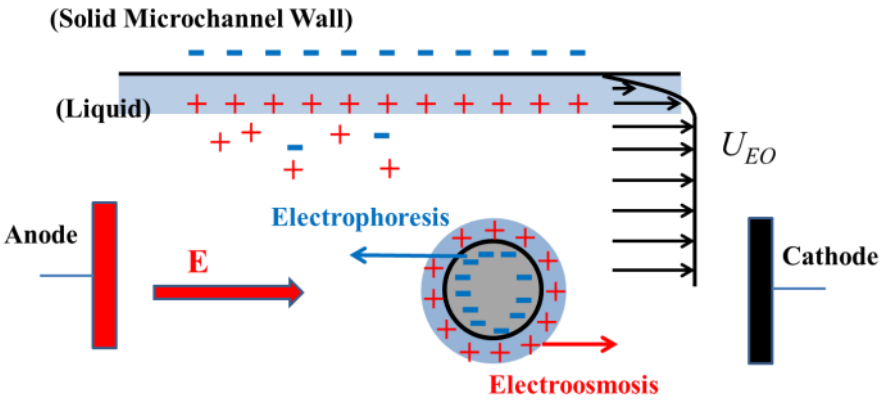

Fig. 1-3: Illustration of the electrophoresis phenomenon close to the particle surface.

Meanwhile, the surface charges on the particle surface respond to the applied electric field, moving the particle towards the opposite direction and such movement of a

*c*harged surface relative to a stationary liquid is termed electrophoresis, a phenomenon that directly determines particle motion. The electrophoretic velocity U_{ep} can be expressed as[17]:

$$U_{ep} = \frac{\varepsilon_f \zeta_p}{\mu_f} E \qquad \text{(Eq. 1-3)}$$

where ζ_p is the surface charge of the particle, E is the electric field strength, and ε_f and μ_f are the permittivity and viscosity of the medium. The actual electrokinetic particle motion is a combined effect of the electroosmosis drag from surrounding counter-ions and the electrophoresis motion of the particle itself.

1.2.4. Dielectrophoresis

Aside from the common electroosmotic and electrophoretic phenomena, another important electrokinetic particle motion occurs when a particle electrolyte solution is exposed to electric field gradients: dielectrophoresis (DEP). This phenomenon happens when there is a difference in the permittivity ε between the particle and the surrounding medium. Particularly, if the particle permittivity ε_p is several orders smaller than the medium permittivity ε_f, then the particle can be deemed as dielectric, and the resulted dielectrophoretic force for a spherical particle under a Direct Current (DC) electric field can be given as[18]:

$$\mathbf{F}_{DEP} = (1/2)\pi\varepsilon_f a^3 f_{CM} (\mathbf{E}\bullet\nabla\mathbf{E}) \qquad \text{(Eq. 1-4)}$$

where a is the particle diameter, and f_{CM} is the Clausius–Mossotti (CM) factor, which depends on the particle and the fluid medium materials. If f_{CM} has a positive value, then

the dielectrophoretic force will direct the particle towards the field-increasing direction, and this motion is called *positive* dielectrophoresis. Similarly, a negative dielectrophoretic force will direct the particle in the opposite direction and is termed *negative* dielectrophoresis.

1.3. Background of Magnetic Phenomena

A magnetic field can be generated easily by permanent magnets or electric currents because it is one of the most universal and abundant natural resources. Generally, a modern neodymium (NdFeB) magnet provides remanent magnetization M_r ~ 1.0-1.4 (T), which measures the magnetization that a ferromagnetic material can generate alone. While on the other hand, for electric current induced magnetic field, the strength and energy depends on the magnitude of the electric current, thus requiring a large input for the electric energy. Both were found to have great uses in industrial, medical, and clinical practices as well as being highly useful for head actuators for computer hard disks, magnetic resonance imaging (MRI), generator, etc.

Based on the response to magnetic field and the nature of the material, magnetic behaviors can be categorized into three classes: ferromagnetic, paramagnetic and diamagnetic. Ferromagnetic materials are the ones that can be strongly attracted to a magnet and retain magnetization. Paramagnetic substances are weakly attracted to a magnet and can be magnetized only if there is an external applied magnetic field applied, they will lose their magnetization once the field source is removed. Diamagnetic objects are often repelled by both poles of a magnet, as their susceptibility χ is usually a negative

value or small enough to be considered negligible. The susceptibility is a dimensionless number that measures the extent of magnetization **M** a material holds in response to an applied magnetic field. The value varies from $1e^{-5}$ for ferromagnetic materials to $-1e^{-10}$ for diamagnetic materials, in SI unit.

1.3.1. Magnetophoresis

Under the applied magnetic field **H**, a mixture of any two materials (usually in aqueous solution) with different susceptibilities will give rise to the magnetophoresis phenomenon. As the two materials own different abilities to maintain magnetization, the material with the higher susceptibility will feel stronger attraction, and orient towards the magnetic field source or the strongest field region. On the other hand, due to the relative attraction motion of higher susceptibility material, the other material with lower susceptibility will be repelled in displacement of the attracted material. Similar to the dielectrophoresis in electrokinetic experiments, this magnetophoretic motion runs with magnetic field gradients. The general magnetophoretic force for a particle is[58]:

$$\mathbf{F}_m = V_p \mu_0 \left(\left(\mathbf{M}_p - \mathbf{M}_f \right) \bullet \nabla \right) \mathbf{H} \qquad \text{(Eq. 1-5)}$$

where V_p is the volume of the particle, $\mu_0 = 4\pi \times 10^{-7}$ H/m is the permeability of free space, $\mathbf{M}_p$ and $\mathbf{M}_f$ are the effective magnetization of the particle and ferrofluid, respectively, and **H** is the magnetic field at the particle center. The direction and magnitude of this magnetic buoyancy force depend on the properties of the actual particle/cell solution pairs.

1.3.2. Positive Magnetophoresis

For cases where $\mathbf{M}_p$ values are larger than $\mathbf{M}_f$ values, the magnetophoretic force in Eq. 1-5 will have a positive value referred to as *positive* magnetophoresis. For example, if magnetic particles or cells with positive susceptibilities (red blood cells) are suspended in diamagnetic solution (water), they will feel the attraction and move towards the magnetic field source.

1.3.3. Negative Magnetophoresis

Contrarily, *negative* magnetophoresis accounts for cases where $\mathbf{M}_p$ values are smaller than $\mathbf{M}_f$ values. For example, if diamagnetic particles or normal cells are distributed into ferrofluids or paramagnetic salts, the particles/cells will be repelled from the magnetic field source.

1.4. Structure of Thesis Work

In the next few chapters, this thesis studies the details of basic and advanced particle manipulations using electrokinetic and magnetic approaches. Chapter 2 elaborates on the fundamental electrokinetic deflection of particles in electrophoresis using wall-induced forces. Chapter 3 further implements the deflection into a three-dimensional focusing of particles. Chapter 4 introduces the diamagnetic particle deflection in ferrofluids and parametric study on the controlling effects. Next, Chapter 5 utilizes the magnetophoretic deflection with the aid of sheath flow to obtain a three-dimensional particle focusing in a T-shaped microchannel. Finally, in Chapter 6 the same

T-shaped microchannel is shown to work in reverse direction to realize particle separation in two different separation schemes. Each chapter presents the background and working principles along with numerical simulation results as a validation for the experimental data.

CHAPTER 2 : PARTICLE ELECTROPHORESIS IN STRAIGHT MICROCHANNELS

2.1. Background on Electrophoretic deflection

Conventional electrophoretic deflection methods often utilize transverse dielectrophoresis (DEP) to alter the relative position of the particle in microchannel width or depth directions. However, it has long been ignored that the confined microchannel regions can also provide transverse deflection forces for the particles. The fundamental study of particle electrophoresis in confined microchannels is relevant to many applications including gel electrophoresis[19] and microfluidic particle-handling devices[20]. Owing to the spontaneous charging of most solid surfaces when brought into contact with polar liquids like water [16], the observed particle motion in electrophoresis through microchannels is typically a combination, but not just a simple addition, of particle electrophoresis and liquid electroosmosis[21].

There have been a number of theoretical and experimental papers investigating the wall effects on particle electrophoretic motion in microchannels. These studies can be coarsely divided into two groups. One group encompasses particle electrophoresis in a straight uniform microchannel of, for example, slit, cylindrical, or rectangular shape where the electric field distribution is uniform[22 - 26]. The other is on particle electrophoresis in either a non-uniform[27-30] or a non-straight[31-34] microchannel where electric field gradients are present. In the latter case, particle dielectrophoresis is usually induced. However, such cross-stream motion has, been deemed absent in particle electrophoresis through a straight uniform microchannel.

In basic LOC devices, under the electrokinetic motion, the particle is usually assumed to move along the electric field line, either along or against the electric field direction, depending on which of these two opposite motions is dominant. Nevertheless, its lateral position relative to the microchannel will not change due to the electric field symmetry in the transverse direction, unless an additional force can be imposed or the field symmetry can be broken in the transverse direction.

Recently, Yariv[35] demonstrated through a theoretical analysis that a particle will drift away from a wall under an electric field acting parallel to the wall. This lateral migration, which is superimposed onto the familiar particle electrophoretic motion parallel to the wall, is induced by a non-zero electrical force resulting from the non-uniform electric field around the particle. A similar force was also considered by Young and Li[36] in an earlier theoretical study to determine the equilibrium height of a colloidal particle during electrophoretic motion above a planar wall. It was found that the gap distance between the particle and the planar wall could be on the order of a few microns.

Due to the existence of the microchannel wall that breaks the field symmetry around the particle, a near wall deflection is generated. This work investigated the wall-induced lateral migration in particle electrophoresis through a straight uniform microchannel of rectangular shape and this data is presented in this chapter. From the theoretical equations, an approximate analytical model is developed to study the effects of the key control parameters.

2.2. Experiment

2.2.1. Microchannel Fabrication

The microchannel was fabricated with polydimethylsiloxane (PDMS) using the standard soft lithography method[37]. The details of the fabrication process are given in APPENDICES. Fig. 2-1 shows a picture of the fabricated microchannel used for this study. It consisted of an 8-mm long uniform section in the middle and a 1 mm long diffuser at each end. So the overall length of this straight channel was 10 mm as indicated in the figure. The entire channel owned a rectangular cross-section with a fixed depth of 25 μm. The channel width of the uniform section was 50 μm.

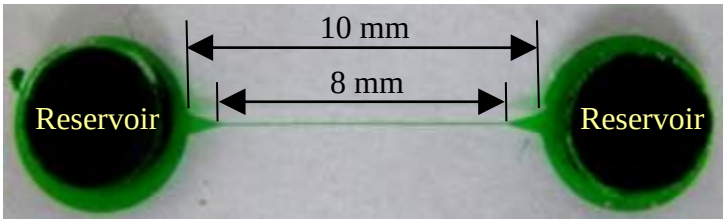

Fig. 2-1: Picture and dimensions of the rectangular microchannel used in the experiment.

2.2.2. Particle Manipulation

Spherical polystyrene particles (Sigma-Aldrich, St. Louis, MO) of two different sizes, 5 μm and 10 μm in diameter, were used in our experiments. The original solution was diluted with 1 mM phosphate buffer to a final concentration of about 10^7 particles per mL for both sized particles. Tween 20 (Fisher Scientific, Hampton, NH) was added at a volume ratio of 0.5% to the particle solutions for reducing the particle adhesions to channel walls.

Electric field was generated by applying a DC voltage drop between the two electrodes in contact with the solution in the reservoirs. The voltages of various magnitudes were supplied by a DC power supply (Glassman High Voltage Inc., High Bridge, NJ). Pressure-driven flow was eliminated by carefully balancing the liquid heights in the two reservoirs prior to each measurement.

2.3. Theory

2.3.1. Deflecting Motion in Particle Electrophoresis

Consider a particle of radius a moving electrophoretically through a rectangular microchannel of half width w_c. The separation distance between the particle and the closer sidewall is assumed to be δ, which in principle may vary from 0 (i.e., in touch with the sidewall) to $(w_c - a)$ (i.e., along the channel centerline). Fig. 2-2 shows the electric field lines and contours (the darker the larger) around the particle in the horizontal plane of the channel. The computation was performed in COMSOL® (Burlington, MA), which will be explained later. Due to the difference in the electric conductivities of the particle and the suspending fluid, electric field becomes non-uniform around the particle. In the channel length direction (i.e., x direction in Fig. 2-2), the electric field distribution is symmetric about the particle, leading to zero electrical force in the particle moving direction.[1] Therefore, the electrokinetic particle motion, $\mathbf{U}_{EK}$ which is a combination of

[1] Note that in the traditional analysis of particle electrophoresis in both bounded and unbounded flows, the electrical force on the neutral system of particle and electrical double layer is assumed to be zero.

particle electrophoresis and fluid electroosmosis as traditionally analyzed [16], [21], remains unaffected.

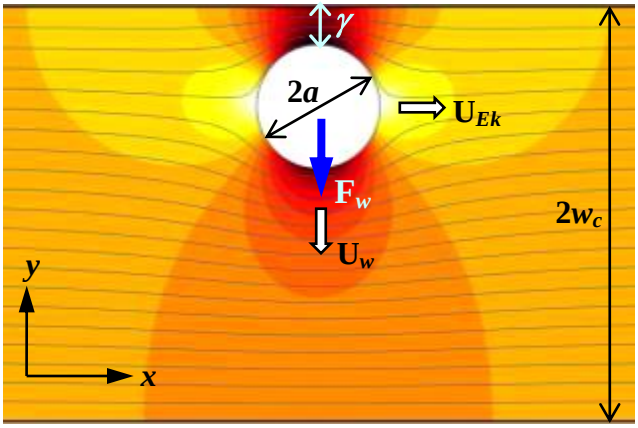

Fig. 2-2: Velocity analysis (in the horizontal plane) of a particle in electrophoretic motion through a rectangular microchannel. The background shows the electric field contours (the darker the larger) and electric field lines.

In the channel width direction (i.e., *y* direction in Fig. 2-2), the particle experiences a net electrical force due to the asymmetric electric field around its two poles. This wall-induced repulsive force [28], [35], [36], $\mathbf{F}_w$, causes a lateral particle migration toward the channel center, denoted as $\mathbf{U}_w$ in Fig. 2-2. Such a lateral migration also takes place in the channel depth direction. It is anticipated that neutrally buoyant particles in electrophoresis should ultimately be traveling along the centerline of a sufficiently long microchannel. In this work, the polystyrene particles were slightly heavier than the suspending fluid and therefore should migrate vertically to an equilibrium position below the channel axis.

2.3.2. Simulation of Particle Trajectory

In simulating the particle trajectory, the following assumptions have been made: (1) particles and channel walls are non-conducting; (2) fluid properties remain uniform throughout the channel; (3) the streamwise electrokinetic motion of particles, $\mathbf{U}_{EK}$, is insensitive to the particle-wall separation distance δ; (4) Reynolds number is very small, and so inertia is negligible; (5) the rotation of a particle does not affect its translation; and (6) particle-particle interaction is negligible.

The instantaneous position of the center of a particle, $\mathbf{r}_p$, is obtained by integrating the particle velocity, $\mathbf{U}_p$, with respect to time, t,

$$\mathbf{r}_p = \mathbf{r}_0 + \int_0^t \mathbf{U}_p(t')dt' \qquad \text{(Eq. 2-1)}$$

where $\mathbf{r}_0$ is the initial position of the particle center and was assumed to be (0, a) in the calculation. In the x direction, the electrokinetic particle velocity is known to vary with the particle-wall separation distance [21]. However, this variation is generally very small unless the particle is nearly in contact with the wall or closely fitting the channel [24], [31], [39], [40]. The former condition is not fulfilled in this work as particles are unable to approach the channel sidewall in close proximity due to the wall-induced repulsive force, $\mathbf{F}_w$ (Fig. 2-2). The condition of closely fitting particles is not applicable in this work because the sizes of the two particles (5 and 10 μm in diameter) are both much smaller than the width of the microchannel (50 μm). Therefore, the streamwise electrokinetic velocity, $\mathbf{U}_{EK}$, is assumed insensitive to the particle-wall separation distance in this approximate analytical model, which is also confirmed by the present and previous experiments[38]. Thus, Eq. 2-1 is reduced to

$$x_p = \mu_{Ek} E t \qquad \text{(Eq. 2-2)}$$

where μ_{Ek} is the electrokinetic particle mobility and E is the externally applied electric field in the uniform channel section.

In the y direction, Eq. 2-2 is rewritten as

$$y_p = \delta + a = \int_0^t U_w(t')dt' \qquad \text{(Eq. 2-3)}$$

where the lateral particle migration velocity, U_w, can be obtained by balancing the wall-induced electrical force, $\mathbf{F}_w$, with the Stokes drag force. The magnitude of this electrical force, F_w, can be determined by integrating the Maxwell stress tensor over the particle surface. Here, the analytical expression provided by Yariv [35] is adapted to account for the net force arising from the two sidewalls,

$$F_w = \frac{3\pi}{16}\left[\left(\frac{a}{\gamma + a}\right)^4 - \left(\frac{a}{2w_v - \gamma - a}\right)^4\right]\varepsilon_f a^2 E^2 \qquad \text{(Eq. 2-4)}$$

where ε_f is the fluid permittivity. Thus, the lateral particle migration velocity can be obtained as

$$U_w = \frac{\varepsilon_f}{32\mu_f} a E^2 \left[\left(\frac{a}{\gamma + a}\right)^4 - \left(\frac{a}{2w_v - \gamma - a}\right)^4\right] \qquad \text{(Eq. 2-5)}$$

where μ_f is the dynamic viscosity of the suspending fluid. In deriving Eq. (5), the Stokes drag coefficient was assumed constant for simplicity, which admittedly breaks down when particles move in close proximity to a channel wall [41]. Apparently U_w increases with the particle size and the applied electric field, but decays rapidly with the increase of the particle-wall separation distance, γ. Additionally it is important to note that the dielectrophoresis-resembled force, $\mathbf{F}_w$, is different from the electrical double layer

interaction between the particle and the wall. The latter force occurs only when γ is in the order of nm[39].

The simulation of particle trajectory was carried out in Matlab® using Eq. 2-3 and Eq. 2-4. The obtained lateral particle position, y_p, at a given location, x_p, of the channel length was then used to calculate the half width, w_p, of the particle stream,

$$w_p = w_c - y_p + a = w_c - \delta . \qquad \text{(Eq. 2-6)}$$

Note that w_p is assumed to be equal to the half channel width, w_c, at $t = 0$. The predicted particle stream width, $2w_p$, is compared with the width of the experimentally recorded particle streaks.

Three parameters were needed in the simulation. First, the electric field in the uniform section of the microchannel in the absence of particles was computed from a 2D model in COMSOL®, which considered the full size of the channel and reservoirs. For example, a 300 V DC voltage drop imposed across the channel length produces an electric field of 34.9 kV/m in the uniform section. Second, the electrokinetic particle mobility, μ_{EK}, was determined by dividing the measured particle velocity in the uniform channel section at an electric field of 34.9 kV/m. This relative small field ensures Joule heating effects were negligible in the 50 μm-wide channel during the measurement[40]. The obtained μ_{EK} is 2.7×10^{-8} $m^2/(V\cdot s)$ for both 5 and 10 μm particles used in the experiment. Third, the properties of the suspending fluid were assumed to be identical to those of water at 20 °C, which include the dynamic viscosity, $\mu_f = 0.9\times10^{-3}$ kg/(m·s) and permittivity, $\varepsilon_f = 6.9\times10^{-10}$ C/(V·m).

2.4. Results and Discussion

2.4.1. Effect of Axial Travelling Distance

Fig. 2-3 shows how the stream width, $2w_p$, of 5 μm particles varies with the axial travelling distance, x_p, during electrophoresis in the uniform section of the straight microchannel. The experimental data (symbols) were obtained by measuring the width of the particle stream in the superimposed images (see the insets and the labeled dimension $2w_p$). Considering the possible error of ±1 pixels in reading the edges of the particle stream, an error bar of ±3.5 μm was added to the experimental data. Due to the wall-induced lateral migration, particles were observed to migrate toward the channel center, leading to a gradually decreased stream width along the channel length. At the entrance of the uniform section (i.e., x_p = 0 in Fig. 2-3, see also the highlight in the inset), the particles appear uniformly distributed forming channel wide stream (i.e., 50 μm). The width of this stream quickly drops to less than 40 μm within the first 1 mm, and then decreases slowly to about 26 μm in the next 7 mm. These varied decreasing trends arise from the fourth-power dependence of the electrical force, i.e., F_w in Eq. 2-4, on the particle-wall separation distance, which are correctly predicted by the analytical model (solid line) in Fig. 2-3. However, the model under-predicts the lateral particle migration due to the approximate treatment of F_w.

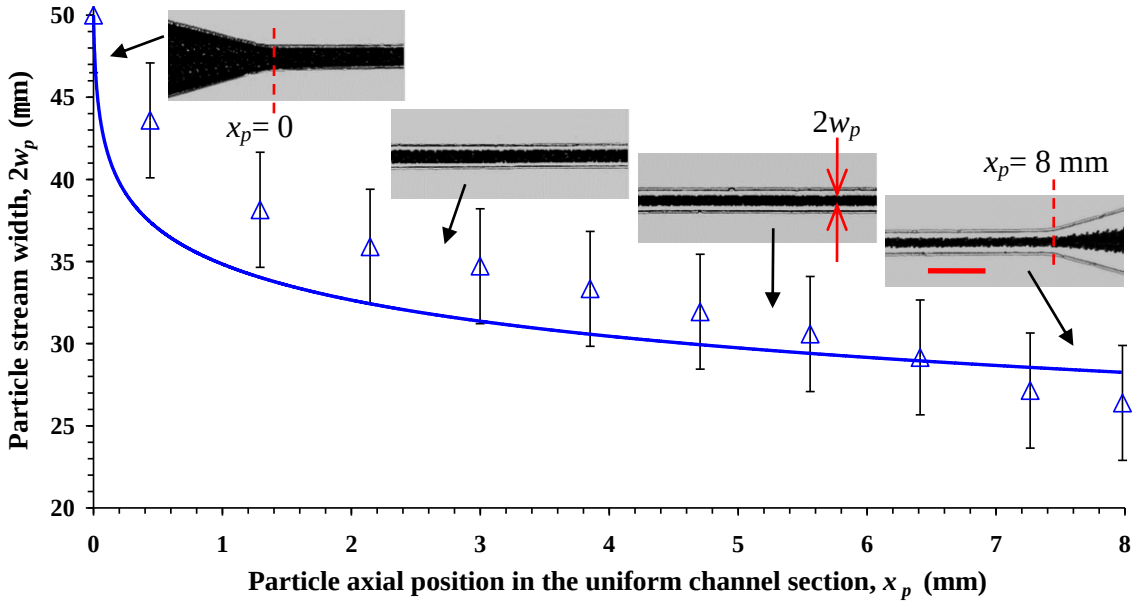

Fig. 2-3: Variation of the stream width, $2w_p$ (see the labeled dimension in the inset), of 5 μm particles with the axial travelling distance in the uniform section of the microchannel under an electric field of 34.9 kV/m. Symbols (with error bars) represent the experimental data while the solid line illustrates the numerically predicted results. The four insets show the superimposed particle images at the entrance, exit, and two intermediate regions of the uniform channel section, respectively. The scale bar represents 100 μm.

2.4.2. Effect of Electric Field

Fig. 2-4 shows the images (left: snapshot; right: superimposed) of 5 μm particles recorded at the exit region of the uniform channel section under different electric fields: (b) 11.6 kV/m, (c) 34.9 kV/m, and (d) 58.2 kV/m. The particle images at the entrance region (Fig. 2-4a) are also included for a clear comparison, which remain nearly the same when the electric field is varied. Obviously increasing the field magnitude enhances the lateral particle migration. This is expected because the width of the particle stream is determined by the ratio of the distance the particle moves laterally to the distance the

particle moves longitudinally, which can be expressed as the ratio of the lateral migration velocity of the particle to the streamwise electrokinetic velocity,

$$\frac{U_w}{U_{EK}} = \frac{\varepsilon_f \left[\left(\frac{a}{a+\gamma} \right)^4 - \left(\frac{a}{2w_c - a - \gamma} \right)^4 \right]}{32\mu_f} \frac{aE}{\mu_{EK}} \qquad \text{(Eq. 2-7)}$$

Since the electrokinetic particle mobility, μ_{EK}, is in general not dependent on the applied electric field, the above velocity ratio increases linearly with electric field, yielding a thinner particle stream along the channel axis as demonstrated in Fig. 2-4.

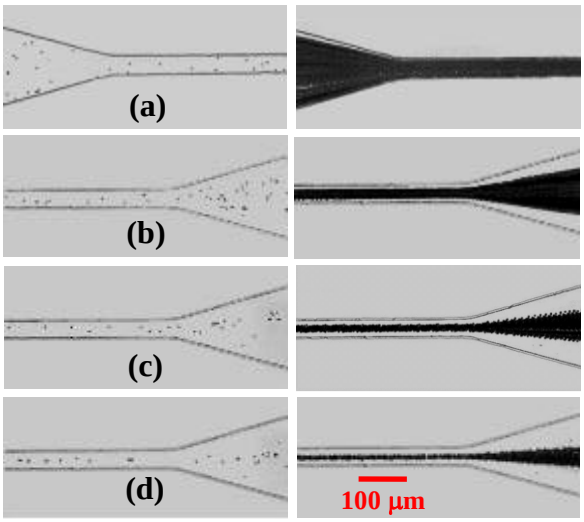

Fig. 2-4: Snapshot (left column) and superimposed (right column) images of 5 μm particles moving at the entrance (a) and exit (b-d) regions of the uniform section of the straight microchannel. The electric fields in (b), (c), (d) are 11.6 kV/m, 34.9 kV/m and 58.2 kV/m, respectively.

The experimentally measured stream widths of 5 μm particles (triangular symbols with error bars) at the exit of the uniform channel section are compared with the

numerically obtained values (the longer solid line) in Fig. 2-5 for a range of electric fields. While it correctly predicts the decreasing trend of the particle stream width with respect to electric field, the model seems to under-predict the lateral particle migration, especially significant at large electric fields. This discrepancy is believed to be the consequence of the approximation of the wall-induced electrical force and the neglect of particle-particle interactions in our model as these two forces both increase with growing electric field.

2.4.3. Effect of Particle Size

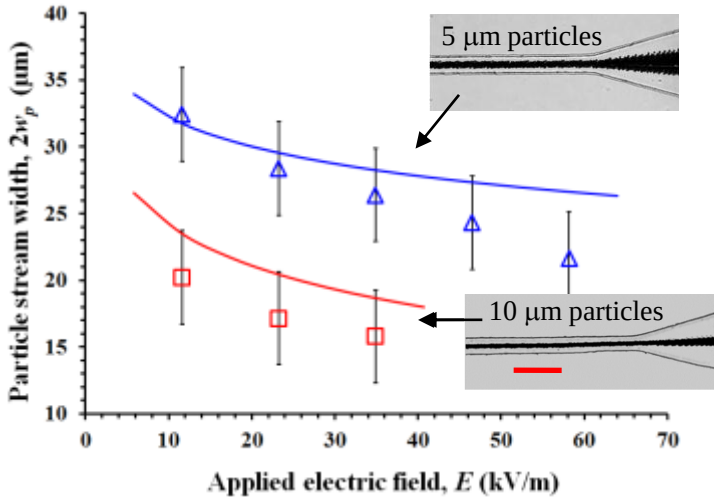

Fig. 2-5: Electric field and particle size effects on the particle stream width at the exit of the uniform section of the microchannel. Symbols (with error bars) represent the experimental data while solid lines are numerically predicted results. The two insets display the superimposed images of 5 and 10 μm particles under the electric field of 34.9 kV/m. The scale bar represents 100 μm.

Fig. 2-5 also illustrates the experimentally (square symbols with error bars) and numerically (the shorter solid line) obtained stream widths of 10 μm particles at the exit

of the uniform channel section at various electric fields. Compared to that of 5 μm particles, the lateral migration of 10 μm particles is much more apparent (see the two inset images in Fig. 2-5). This observation correlates well with the prediction of Eq. 2-7. As the measured electrokinetic mobilities of the two particles are roughly identical, the velocity ratio, U_w/U_{EK}, of 10 μm particles is certainly larger than that of 5 μm particles. At the electric field of 10 kV/m, the lateral migration can already focus 10 μm particles from a 50 μm wide stream at the entrance to a stream of 21 μm wide at the exit of the uniform section. When the electric field increases to 34.9 kV/m, 10 μm particles can only migrate in a single file because the measured particle stream width is decreased to about 15 μm. This focusing phenomenon in particle electrophoresis, which will become more pronounced in a longer microchannel as evidenced in Fig. 2-3, might be potentially used in microfluidic flow cytometry[41],[42],[43]. In addition, similar to what was discussed earlier for 5 μm particles, the numerical model also under-predicts the lateral migration of 10 μm particles.

It was suspected that under actual experimental conditions, particles also experience top and bottom wall-induced forces, especially when the particles were close or in contact with these walls. It is not simply a two-dimensional force combination in the channel width direction. However, the analytical force expression was based on the assumption that the particle is in vicinity of an infinite wall, which in this case the aspect ratio for channel cross section is only 2:1 and, the particle motion was greatly affected by the top and bottom wall. This became the main reason that analytical prediction always under-predict the particle deflections.

2.5. Conclusions

Similar but still different to the dielectrophoresis, the wall-induced repulsive force acts on the particle as the electric field symmetry is broken by the existence of the bounded surface, which creates non-uniform electric field around the particle in the transverse direction. This wall-induced cross-stream motion has been observed to gradually focus 5 and 10 μm-diameter polystyrene particles to a stream flowing in the center region of a 50 μm-wide rectangular microchannel. The fundamental study shows that the width of the particle stream at the channel exit decreases with the increase in either particle size or electric field. The measured values of the stream width are in reasonable agreement with the predictions of an approximate analytical model. It is envisioned that the lateral particle migration in microchannel electrophoresis may be utilized to implement a three-dimensional focusing of cells for the application of microflow cytometry.

CHAPTER 3 : THREE-DIMENSIONAL PARTICLE FOCUSING IN ELECTROPHORESIS

3.1. Background on Electrokinetic Focusing

It was found that particle motion in a bounded region would experience a repulsive force from the solid surface. The observed result is that particles in electrophoresis through a straight rectangular microchannel migrated toward the centerline in the horizontal plane. This effect grew stronger with an increasing particle size or increasing electric field strength, especially when the particle was close to the microchannel wall. Moreover, the suspended particle not only feels the wall-induced repulsion from the two side walls, but also the same influences from the top and bottom walls when the field symmetries are broken in the depth direction. Therefore, by utilizing the repulsive forces in both channel width and depth directions, three-dimensional particle focusing can be realized in a rectangular microchannel.

Focusing particles into a tight stream is usually a necessary step prior to counting, detecting, and sorting [1]. As traditionally defined, particles can be focused in either two-dimension (normally horizontal direction) or three-dimension (both horizontal and vertical directions). A two-dimensional focusing is usually sufficient for continuous-flow particle sorters [3]. For the application to flow cytometers, however, three dimensional focusing is necessary to enhance the electrical or optical detection [44], [45], [46]. It can also suppress particle adhesions to microchannel walls.

A variety of particle focusing methods have been developed in microfluidic devices. These methods can be categorized into the two genres of active and passive

particle focusing. Active particle focusing often requires expensive peripheral instruments and/or complex channel designs, such as the elliptic-like and planar electrode arrays used by Yu *et al.* [47] and Chu *et al.* [48], respectively. Passive technique, on the other hand, provides multiple alternatives but is still deficient in some respects. For example, insulator-based dielectrophoresis (iDEP) has been demonstrated to pump and focus particles concurrently [33] but this is prone to fouling due to surface impurity [49] and Joule heating [50], [51]. Additionally, curvature-induced dielectrophoresis (C-iDEP) recently developed a passive electrokinetic method to focus particles in serpentine [33] and spiral [34] microchannels. However, this method provides only a two-dimensional focusing in the width direction of long microchannels. Aside from the above focusing methods, the wall-induced repulsion introduced in previous chapter may provide a simple but effective three-dimensional particle focusing.

3.2. Experiment

The microchannel used was 2 cm long with a uniform cross-section of 50×50 μm. It was fabricated with polydimethylsiloxane (PDMS) using the standard soft lithography method. In these experiments, polystyrene particles of 5 and 10 μm in diameter (Sigma-Aldrich) were re-suspended in a solution with neutral buoyancy to a concentration of about 10^7 particles per mL. The solution was made by mixing 1 mM phosphate buffer and glycerol at a volume ratio of 7.8:2.2 [52] to achieve a mass density that matches that of the particles. The particle transport was driven by a DC electric field supplied by a power supply (Glassman High Voltage Inc., High Bridge, NJ), and visualized with a CCD

camera (Nikon DS-Qi1Mc) through an inverted microscope (Nikon TE2000U, Nikon Instruments, Lewisville, TX).

3.3. Theory

The finite-size particle distorts the electric field lines, resulting in electric field gradients formed (see the field contour over the channel cross-section in Fig. 3-1). The presence of the channel walls break the symmetry of the field gradients, which yields an electrical force, $\mathbf{F}_w$, pointing away from the nearby walls [35], [36]. As a consequence, particles of neutral buoyancy ultimately are pushed toward the center of the channel cross-section, forming a three-dimensionally focused stream along the channel axis. The effectiveness of this electrokinetic focusing is determined by the ratio of the distance the particle moves laterally to the distance it travels longitudinally. Equivalently this focusing depends on the ratio of the $\mathbf{F}_w$-induced velocity to electrokinetic particle velocity and the ratio of channel length to width (or the hydraulic diameter). The dielectrophoresis-resembled force, $\mathbf{F}_w$, decays rapidly when the particle is away from the channel wall(s), but increases quadratically with both particle size and applied electric field [35], [36]. Therefore, the induced lateral particle migration is proportional to the particle size and the electric field squared. In contrast, the electrokinetic particle velocity is a linear function of the electric field [21] while insensitive to the particle size unless the particle closely fits the channel [40]. Hence, increasing the electric field and/or particle size should in principle enhance the wall-induced electrokinetic particle focusing.

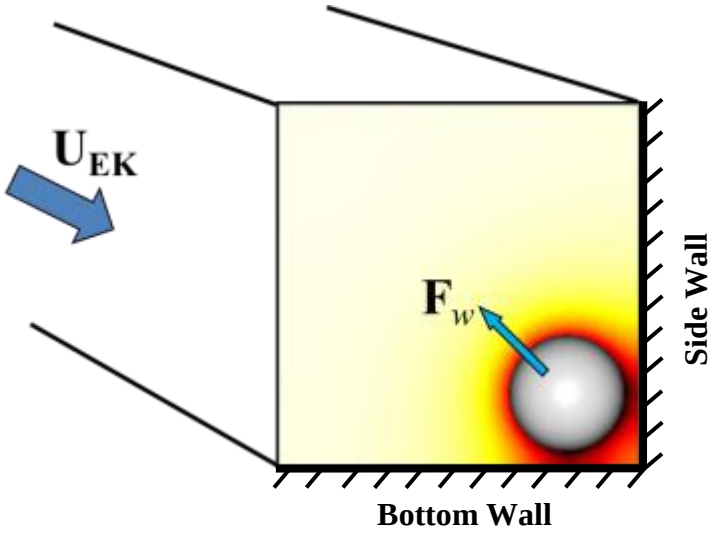

Fig. 3-1: The non-uniform electric field around a particle (indicated by the background contour that was obtained from COMSOL®, the darker the larger) generates an electrical force, $\mathbf{F}_w$, pushing the particle away from the nearby walls to the center of the channel cross-section.

3.4. Results and Discussion

Fig. 3-2 shows the snapshot top-view images of 10 μm particles flowing through the inlet (a), middle (b), and outlet (c) of the rectangular microchannel. The applied DC voltage drop across the 2-cm long channel was 400 V, producing a 23.3 kV/m electric field. The focal plane of the microscope objective was positioned approximately to the middle of the channel depth. At the channel inlet, both off-centered (in the horizontal or channel width direction, highlighted with squares for clarity) and defocused (in the vertical or channel depth direction, highlighted with circles for clarity) particles are shown in Fig. 3-2a. This is attributed to the uniform spreading of neutrally buoyant particles in the upstream reservoir. When particles travelled through half of the channel length, defocused particles are observed infrequently (Fig. 3-2b) and most are moving in

a narrow region about the channel centerline. Further, in Fig. 3-2c neither off-centered nor defocused particles are seen, indicating that three-dimensional particle focusing formed at the channel outlet. This trend demonstrates that the autonomous focusing of particles in electrophoresis through a rectangular microchannel increases with channel length.

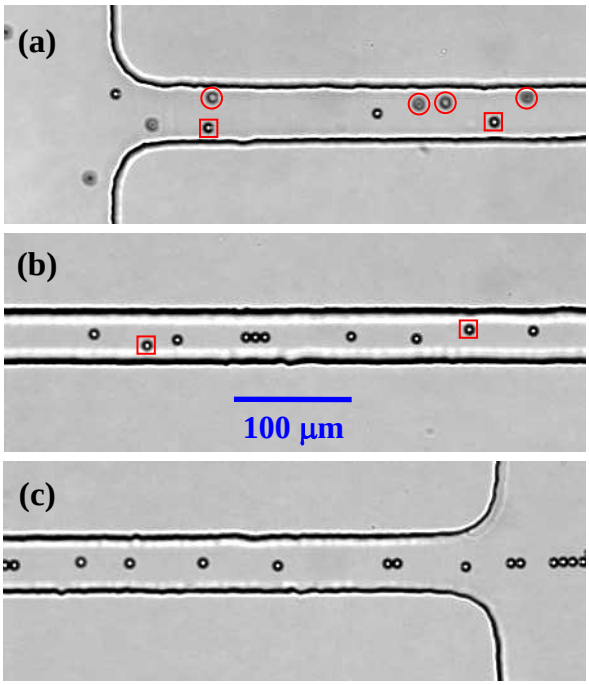

Fig. 3-2: Snapshot top-view images of 10 μm particles moving through the inlet (a), middle (b), and outlet (c) of a rectangular microchannel at the electric field of 23.3 kV/m. For clarity the off-centered and defocused particles in (a) and (b) are highlighted with boxes and circles, respectively. The flow direction is from left to right.

Fig. 3-3 compares the snapshot images of 5 μm particles at the outlet of the rectangular microchannel under different electric fields. The particle image at the channel inlet is also included in Fig. 3-3a for a clear comparison, where, once again, both off-

centered (highlighted with squares for clarity) and defocused (highlighted with circles for clarity) particles are present. As expected, electrokinetic particle focusing is enhanced with the rise of the electric field. Specifically, at the 11.6 kV/m electric field, many particles are still off-centered and defocused at the channel outlet while at a lesser extent than at the inlet. This is identified from the clear edges of most particles in Fig. 3-3b. When the electric field is increased to 34.9 kV/m, an apparently better focusing is obtained in the channel width (or horizontal) direction because much less off-centered particles are observed (Fig. 3-3c). However, the improvement in the vertical particle focusing is not as evident as in the horizontal focusing due to the limited depth of focus of the optical microscope. As the electric field further increases to 58.2 kV/m, a tightly focused particle stream is observed along the channel centerline (Fig. 3-3d) where few defocused particles are present.

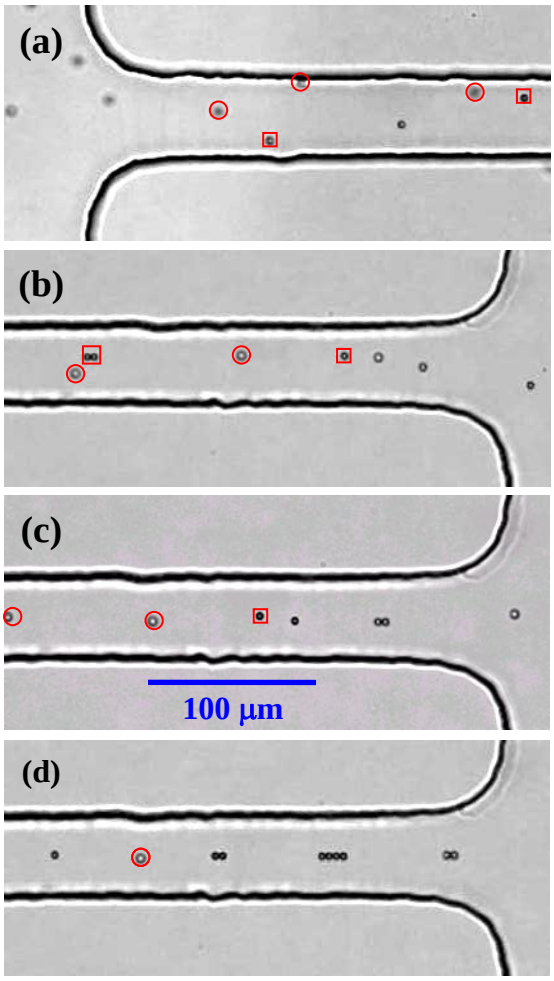

Fig. 3-3: Snapshot top-view images showing the electric field effect on the three-dimensional focusing of 5 μm particles at the outlet of a rectangular microchannel: (b) 11.6 kV/m, (c) 34.9 kV/m, and (d) 58.2 kV/m. The particle image at the channel inlet is shown in (a). For clarity the off-centered and defocused particles are highlighted with squares and circles, respectively. The flow direction is from left to right.

Fig. 3-4 compares the widths of the focused 5 and 10 μm particle streams at the channel outlet with respect to the applied electric field. The data points (symbols, averaged over three measurements for each size of particles) were obtained by measuring the widths of the particle trajectories in the superimposed images (see the inset sample

images in Fig. 3-4. Apparently, 10 μm particles gain a better focusing than 5 μm particles, where the measured stream width of the former is on-average 30% smaller for the range of an 11.6 to 34.9 kV/m electric field. This is because 10 μm particles experience a larger wall-induced lateral velocity than 5 μm particles while their electrokinetic velocities are nearly identical. The measured electrokinetic mobility (i.e., electrokinetic velocity per unit field) is about 1.1×10^{-8} $m^2/(V\cdot s)$. In addition, similar to what was seen in Fig. 3-3, increasing the electric field leads to a reduction of the stream width for both sizes of particles.

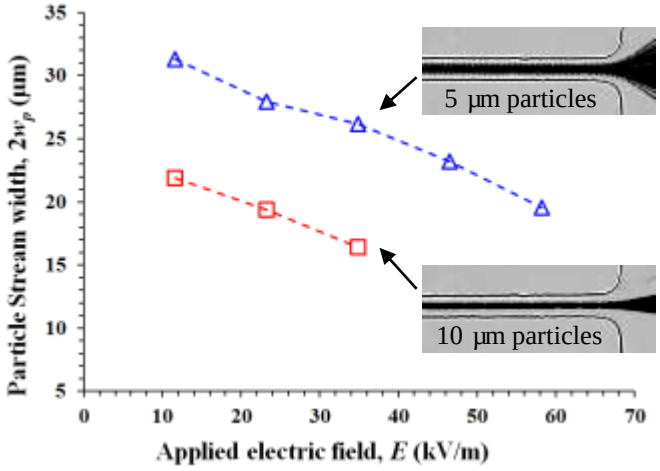

Fig. 3-4: Electric field and particle size effects on the width of the focused particle stream at the outlet of a rectangular microchannel. The lines are used solely to guide the eyes. The two insets display the superimposed images at the 34.9 kV/m electric field.

3.5. Conclusions

In summary, the wall-induced deflection was determined to provide a three-dimensional electrokinetic focusing of particles in a straight rectangular microchannel.

Due to the wall-induced electric repulsion force, neutrally buoyant particles in electrophoresis were observed to migrate toward and travel along the channel axis. This cytometric application prevents the vertical particle deposition and adhesions to the channel wall. Non-neutral particles are anticipated to flow in a focused stream near the top or bottom wall, onto which sensing electrodes may be fabricated for improved electrical detections [53]. Such autonomous particle focusing in a rectangular microchannel may potentially be used in microflow cytometry.

CHAPTER 4 : PARTICLE MAGNETOPHORESIS IN STRAIGHT MICROCHANNELS

4.1. Background on Magnetic manipulation

Magnetic field-induced particle control via permanent magnets is accepted as the simplest and cheapest manipulation method. Compared to the electrokinetic method demonstrated in the previous chapters, the magnetic method does not bring the field source (permanent magnets) into contact with the fluids, and it is thus free of heating, pH value and ionic concentration issues that accompany electrokinetic techniques. In common magnetic techniques, a neodymium (NdFeB) magnet is sufficient to provide a strong magnetic field. Such a magnet is typically so small that it can be embedded inside the PDMS material and reduces the cost by a few dollars.

This method is based on magnetophoresis that directs particles either along or against the magnetic field gradient. In the former, magnetic particles suspended in nonmagnetic solutions experience *positive* magnetophoresis and are attracted towards the highest magnetic region [54]. While in *negative* magnetophoresis, the diamagnetic particles, which cover the majority of synthetic and biological particles suspended in magnetic solutions, are repelled from the magnet due to the magnetic buoyancy force [55]. Two types of magnetic solutions have been used for this purpose and they are paramagnetic salts and ferrofluids. Common paramagnetic solutions such as $MnCl_2$ and $GdCl_3$ have a weak magnetic susceptibility[56] and these rely on either high salt concentration or strong magnet(s) (e.g., a superconducting magnet[57]) to enhance magnetic effect. While high salt concentration renders the paramagnetic solution non-

biocompatible[58] and the magnet(s) must be brought very close to the suspended diamagnetic particles[59] to generate large magnetic field gradients, either of these requirements greatly increases the difficulty for magnetic particle manipulation within on-chip planar microchannels.

Alternatively, ferrofluids are opaque colloidal suspensions of magnetic nanoparticles (made of magnetite, Fe_3O_4, and usually of 10 nm in diameter) in pure water or organic oil with surfactants coating to prevent agglomerations [60]. They usually have a magnetic susceptibility that is several orders of magnitude larger than paramagnetic solutions. Therefore, regular permanent and electric magnets normally suffice to induce *negative* magnetophoresis for manipulating diamagnetic particles of varying sizes[61],[62].

In this chapter, a comprehensive study of diamagnetic particle motion in ferrofluid microchannel flows in a rectangular straight microchannel is presented. The deflection motion provides the fundamental knowledge on particle transport in *negative* magnetophoresis and prepares preconditions for particle focusing. The particle transport is investigated in both the horizontal and vertical planes of a rectangular microchannel that demonstrates a three-dimensional particle deflection due to the induced negative magnetophoresis. This chapter also presents a three-dimensional analytical model developed to understand the observed particle behavior in ferrofluid flows, which is validated by the acquired experimental results.

4.2. Experiment

4.2.1. Microchannel Fabrication

Fig. 4-1a shows a picture of the microfluidic device used in this experiment. The straight microchannel (filled with the black-brown ferrofluid) is 2 cm long, 200 μm wide and 70 μm deep. The microchannel was fabricated with PDMS using the standard soft lithography method. Prior to dispensing liquid PDMS over the channel master, a prism was positioned 500 μm away from the edge of the microchannel to achieve the side-view imaging and was fixed to the substrate using a sticky tape. The cured PDMS along with the embedded prism was then carved out and bonded to a glass slide forming the microfluidic chip. In the half of the chip without the prism, part of the PDMS was cut out wherein a neodymium (NdFeB) permanent magnet (B221, K&J Magnetics, Inc. Plumsteadville, PA) was placed with its bottom surface in contact with the glass slide. The distance between the magnet and the microchannel can be varied during the experiment. The magnet has a dimension of 1/8"×1/8"×1/16" thick, and is magnetized through thickness that is perpendicular to the microchannel or the flow direction in the experiment.

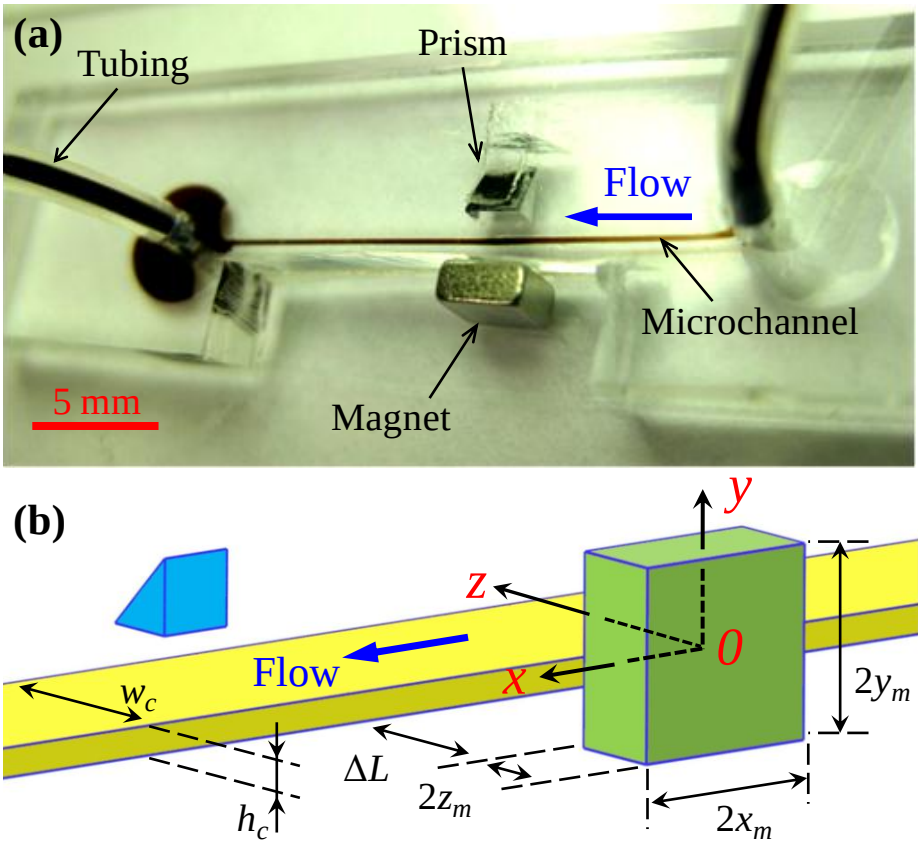

Fig. 4-1: Picture of the microfluidic device used in the experiment (a), and schematic of the magnet-microchannel system with coordinates and dimensions indicated (b). The coordinate system originates from the center of the permanent magnet whose magnetization direction is in line with coordinate *z*.

4.2.2. Preparation of Particle Suspensions

EMG 408 ferrofluid was purchased from Ferrotec Corp (Santa Clara, CA). It contains 1.2% magnetic nanoparticles in volume with a reported viscosity of 1.2×10^{-3} kg/m/s[63], and has a saturation magnetization of 5252 A/m (corresponding to 6.6 mT as per the manufacturer). Green fluorescent polystyrene particles of 2.2 μm, 5 μm and 10 μm in diameters were obtained from Duke Scientific Corp. They are all packaged as 1% solids in water with size non-uniformity being less than 5%. Each type of these

diamagnetic micro-particles was re-suspended in either the original or a diluted ferrofluid to a final concentration of about 1×10^6 particles/ml. The 0.5× (i.e., 0.6% magnetic nanoparticles in volume) and 0.25× (i.e., 0.3% vol.) dilutions were made by mixing the original ferrofluid with the same and the triple volume of de-ionized water, respectively. The suspension of 5 μm particles in 0.5× ferrofluid was used as a reference solution for the experiment.

4.2.3. Particle Manipulation

The particle suspensions in ferrofluids were driven through the microchannel by an infusion syringe pump (NE-300, New Era Pump Systems, Inc., NY). Teflon tubing (1622L, Upchurch Scientific) was used to connect the pump to the channel and transfer the solution out of the channel.

4.3. Theory

4.3.1. Magnetic Force

The magnetic "buoyancy" force, $\mathbf{F}_m$, on a diamagnetic particle suspended in a magnetic fluid is given by [10],[64]

$$\mathbf{F}_m = -V_p \mu_0 \left(\mathbf{M}_f \bullet \nabla\right)\mathbf{H} \qquad \text{(Eq. 4-1)}$$

where V_p is the volume of the particle, $\mu_0 = 4\pi\times10^{-7}$ H/m is the permeability of free space, $\mathbf{M}_f$ is the effective magnetization of the ferrofluid that is typically orders of magnitude larger than that of diamagnetic particles, and **H** is the magnetic field at the particle center. Note that Eq. 4-1 is valid only when the variation of the applied magnetic field over the

particle volume can be neglected. This assumption is fulfilled in the current work as the permanent magnet is distant from the microchannel and the particles are small in size. The former fact also enables us to neglect the influence of the magnetic field on the concentration of magnetic nanoparticles in the ferrofluid, i.e., the volume fraction of nanoparticles, ϕ, is assumed homogeneous in the following analysis.

The magnetization of ferrofluids, $\mathbf{M}_f$, is collinear with the static magnetic field, **H**, produced by a permanent magnet, and its magnitude, M_f, can be determined using the Langevin function, $L(\alpha)$, if the volume fraction of magnetic nanoparticles, ϕ, is low[65],

$$\frac{M_f}{\phi M_d} = L(\alpha) = \coth(\alpha) - \frac{1}{\alpha} \qquad \text{(Eq. 4-2)}$$

$$\alpha = \frac{\pi \mu_0 M_d H d^3 M_f}{6 k_B T} \qquad \text{(Eq. 4-3)}$$

where M_d = 4.379×10^5 A/m is the saturation moment of the magnetic nanoparticles as calculated from the manufacturer-provided saturation magnetization of the ferrofluid, M_{sat} (= 5252 A/m for EMG 408 with ϕ = 1.2%), through $M_d = M_{sat}/\phi$. Other symbols in Eq. 4-3 include H, the magnetic field magnitude, d, the average diameter of the magnetic nanoparticles, k_B, the Boltzmann constant, and T, the ferrofluid or particle temperature. The components of $\mathbf{M}_f$ along the three directions, M_i (i = x, y, z), can be related to those of **H**, i.e., H_i (i = x, y, z), through:

$$M_i = M_f \frac{H_i}{H} \qquad \text{(Eq. 4-4)}$$

Theoretically the ferrofluid (and the diamagnetic micro-particles as well) should disturb the external magnetic field due to its dissimilar permeability from free space.

However, this perturbation is essentially small for dilute ferrofluids. Therefore, this work can employ Furlani's analytical model[66] to determine the three-dimensional magnetic field, **H** = (H_x, H_y, H_z), of a rectangular magnet whose magnetization direction is in line with z coordinate,

$$H_x(x,y,z)=\frac{M_s}{4\pi}\sum_{i=1}^{2}\sum_{j=1}^{2}(-1)^{i+j}\ln\left\{\frac{(y-y_1)+\left[(x-x_i)^2+(y-y_1)^2+(z-z_j)^2\right]^{1/2}}{(y-y_2)+\left[(x-x_i)^2+(y-y_2)^2+(z-z_j)^2\right]^{1/2}}\right\}$$

(Eq. 4-5)

$$H_y(x,y,z)=\frac{M_s}{4\pi}\sum_{i=1}^{2}\sum_{j=1}^{2}(-1)^{i+j}\ln\left\{\frac{(x-x_1)+\left[(x-x_1)^2+(y-y_i)^2+(z-z_j)^2\right]^{1/2}}{(x-x_2)+\left[(x-x_2)^2+(y-y_i)^2+(z-z_j)^2\right]^{1/2}}\right\}$$

(Eq. 4-6)

$$H_z(x,y,z)=\frac{M_s}{4\pi}\sum_{i=1}^{2}\sum_{j=1}^{2}\sum_{k=1}^{2}(-1)^{i+j+k}\tan^{-1}\left\{\frac{(x-x_i)(y-y_j)}{(z-z_k)\left[(x-x_i)^2+(y-y_j)^2+(z-z_k)^2\right]^{1/2}}\right\}$$

(Eq. 4-7)

where M_s = 1.05×10^6 A/m is the residual magnetization of the permanent magnet as calculated from the residual magnetic flux density, B_s (= 1.32 T as per the manufacturer) through $M_s = B_s/\mu_0$. Other symbols involved in the magnetic field equations are $x_1 = x_m$, $x_2 = -x_m$, $y_1 = y_m$, $y_2 = -y_m$, $z_1 = z_m$, and $z_2 = -z_m$ where x_m, y_m and z_m represent one half of the dimensions of the magnet in the x, y, and z directions, respectively. The coordinates and dimensions for the magnet-microchannel system are illustrated in Fig. 4-1b. Note that the coordinate system originates from the magnet center.

4.3.2. Deflecting Motion in Particle Magnetophoresis

The presence of the negative sign in Eq. 4-1 indicates that the magnetic force, $\mathbf{F}_m$, directs diamagnetic particles in ferrofluids along the direction of the decreasing magnetic field. Using Eq. 4-5, Eq. 4-6 and Eq. 4-7, this work determined the magnetic field distribution with the channel for the current magnet-microchannel system (see Fig. 4-1). Table 1 summarizes the parameters used in the calculation. Fig. 4-2 shows the magnetic field contours in the horizontal plane at $y = h_c/2$ with h_c the microchannel height (left plot) and the vertical plane at $x = 0$ (right plot) of the microchannel (see Fig. 4-1b for the coordinates). It is evident that the permanent magnet generates magnetic field gradients in all three directions. Specifically in the horizontal plane (i.e., x-z plane, left), diamagnetic particles should be deviated from the x-direction ferrofluid flow and deflected along the positive z direction toward the channel sidewall that is farther from the magnet. Meanwhile in the vertical plane (i.e., y-z plane, right), the particles should also be deflected along the negative y direction toward the bottom channel wall, i.e., downwards from the magnet center. These two phenomena are schematically illustrated in Fig. 4-2 via the force analysis on a single particle, where $\mathbf{F}_s$ denote the Stokes drag force.

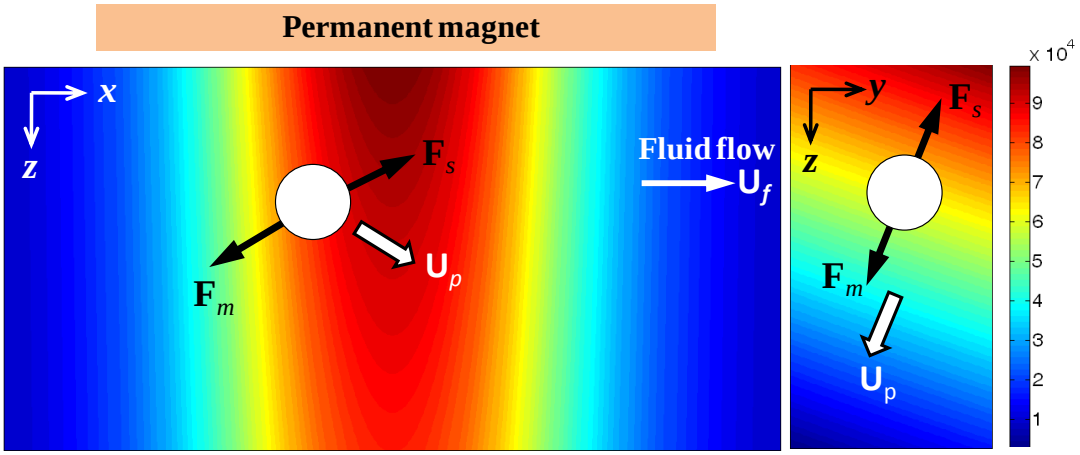

Fig. 4-2: Force analyses on a diamagnetic particle in ferrofluid field flow in the horizontal (left, partial view) and vertical (right, i.e., the channel cross-sectional view) planes of the microchannel. The background shows the contour of magnetic field strength in the absence of the diamagnetic particle. The microchannel and magnet are not drawn to scale.

Table 1: List of the parameters used in the analytical model. Some of the parameters are varied in the experiment, and their specific values are referred in the text.

Parameter		**Description**	**Value**	**Unit**
Magnet	M_s	Residual magnetization	1.05×10^6	A/m
	x_m	Half length	3.175	mm
	y_m	Half height	3.175	mm
	z_m	Half thickness	1.588	mm
	ΔL	Distance between the magnet and the channel edge	1.33	mm
Ferrofluid	ϕ	Volume fraction of magnetic nanoparticles	1.20% for original	
	M_d	Saturation moment of magnetic nanoparticles	4.379×10^5	A/m
	d	Mean diameter of magnetic nanoparticles	10	Nm
	η	Dynamic viscosity	1.2×10^{-3} for original	Kg/m/s
Diamagnetic particles	a	Particle radius	Three sizes used: 1.1, 2.5 and 5	μm
Microchannel	w_c	Channel width	200	μm
	h_c	Channel Height	70	μm
	Q	Volume flow rate	480	μL/hr

The above analysis is also supported by the axial distribution of the magnetic force, $\mathbf{F}_m$, on a 5 μm diamagnetic particle along the channel centerline as demonstrated in Fig. 4-3. Other parameters involved in the calculation are summarized in Table. 1. The *z*-component force, $F_{m,z}$, and the *y*-component force, $F_{m,y}$, acquire a positive and negative value, respectively, within ~3 mm distance before and after the magnet (i.e., –5 mm < x < +5 mm). They both reach the extreme when the particle is on the center-plane of the magnet, i.e., $x = 0$. Similarly, the *x*-component magnetic force, $F_{m,x}$, also obtains a non-zero value in the same range of *x*. It, however, varies from negative (which hinders the particle motion) in the upstream half of the magnet to positive (which propels the particle)

in the downstream half. The ultimate consequence of these negative magnetophoretic motions is a three-dimensionally focused particle stream flowing near the outer bottom corner of the microchannel, the farthest place from the center of the magnet.

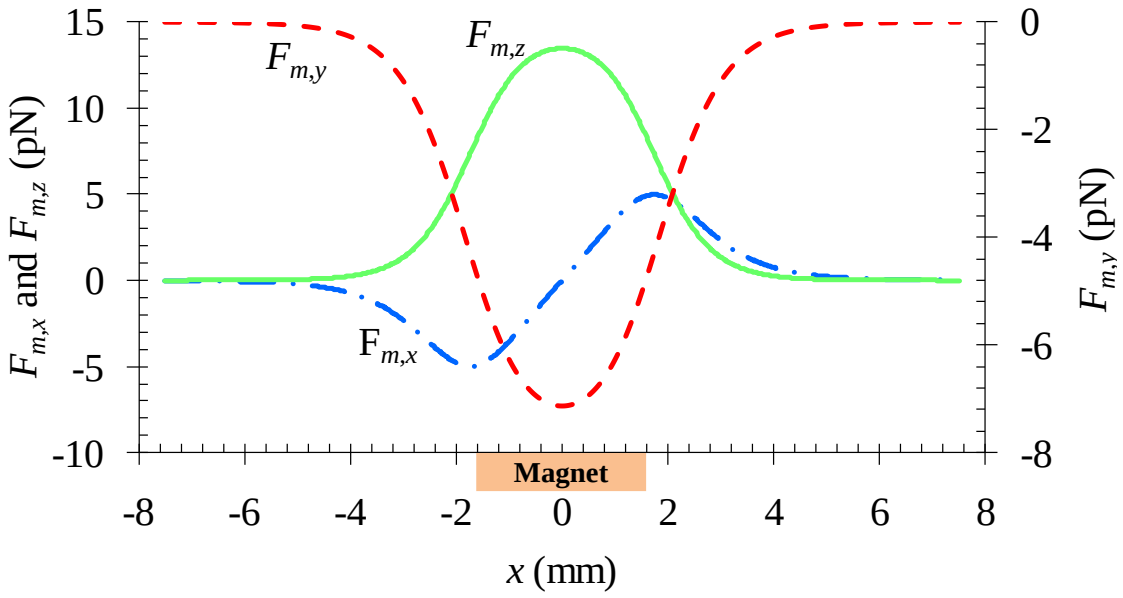

Fig. 4-3: Axial variations of the three components of the magnetic force, $\mathbf{F}_m$, along the centerline of the microchannel. The location of the permanent magnet is highlighted in the plot.

The magnetic *deflection* of diamagnetic particles in ferrofluid flows is determined by the ratio of the particle velocities, $\mathbf{U}_p$, perpendicular and parallel to the flow,

$$deflection_i = \frac{U_{p,i}}{U_{p,x}} = \frac{U_{m,i}}{U_f + U_{m,x}} \qquad (i = y, z) \qquad \text{(Eq. 4-8)}$$

where U_f is the axial flow velocity given by[67]

$$U_f = \frac{Q\pi}{2w_c h_c}\left\{\left[1-\frac{\cosh\left(\frac{\pi z'}{h_c}\right)}{\cosh\left(\frac{\pi w_c}{2h_c}\right)}\right]\cos\left(\frac{\pi y'}{h_c}\right)-\frac{1}{27}\left[1-\frac{\cosh\left(\frac{3\pi z'}{h_c}\right)}{\cosh\left(\frac{3\pi w_c}{2h_c}\right)}\right]\cos\left(\frac{3\pi y'}{h_c}\right)\right\}\bullet \quad \text{(Eq. 4-9)}$$
$$\left\{\left[1-\frac{2h_c}{\pi w_c}\tanh\left(\frac{\pi w_c}{2h_c}\right)\right]+\frac{1}{81}\left[1-\frac{2h_c}{3\pi w_c}\tanh\left(\frac{3\pi w_c}{2h_c}\right)\right]\right\}^{-1}$$

and where Q is the volume flow rate of the particle suspension through the microchannel of width w_c and height h_c. The auxiliary coordinates y' and z' originate from the center of the channel cross-section and are parallel to the y and z coordinates for the magnet (see Fig. 4-1b), respectively. Note that Eq. 4-9 contains only the first two terms in the general formula for simplicity, which is found to cause less than 1% error[63].

The magnetophoretic particle velocity, $\mathbf{U}_m$, in Eq. 4-8 can be obtained by balancing the magnetic force, $\mathbf{F}_m$, in Eq. 4-1 with the Stokes drag force (i.e., $\mathbf{F}_s$ in Fig. 4-2), yielding

$$\mathbf{U}_m = \frac{\mathbf{F}_m}{6\pi\eta a f_D} = \frac{-\mu_0\phi a^2}{9\eta f_D}\frac{M_d L(\alpha)\nabla\mathbf{H}^2}{H} \quad \text{(Eq. 4-10)}$$

where η is the dynamic viscosity of the ferrofluid, a is the radius of the spherical diamagnetic particle, and f_D is the drag coefficient accounting for the particle-wall interactions[68]. Eq. 4-1 and Eq. 4-2 were used to obtain the term after the second equal sign in Eq. 4-10. The fraction involving magnetic field is derived based on the fact that the ferrofluid magnetization, $\mathbf{M}_f$, is collinear with the static magnetic field, $\mathbf{H}$. Therefore, the diamagnetic particle deflection should increase with increasing ferrofluid concentration, ϕ, and particle size, a. In addition, lowering the ferrofluid flow velocity (or flow rate) should also enhance the particle deflection according to Eq. 4-8. As the width

of the microchannel is nearly three times the depth, this work considers only the retardation effects from the top or the bottom wall whichever is closer to the particle. Moreover, for particle motions parallel (i.e., along the *x*- and *z*-directions, see Fig. 4-1b) and normal (i.e., along the *y*-direction) to the top/bottom wall, this work uses a different formulae for f_D[41],

$$f_{D,\parallel} = \left[1 - \frac{9}{16}\left(\frac{a}{\delta}\right) + \frac{1}{8}\left(\frac{a}{\delta}\right)^3 - \frac{45}{256}\left(\frac{a}{\delta}\right)^4 - \frac{1}{16}\left(\frac{a}{\delta}\right)^5\right]^{-1} \qquad \text{(Eq. 4-11)}$$

$$f_{D,\perp} = \left[1 - \frac{9}{8}\left(\frac{a}{\delta}\right) + \frac{1}{2}\left(\frac{a}{\delta}\right)^3\right]^{-1} \qquad \text{(Eq. 4-12)}$$

where δ is the smaller value of the separation distances from the particle center to the top and the bottom channel walls, respectively.

4.3.3. Simulation of particle trajectory

Based on the above analysis, this work developed a 3D analytical model to simulate the trajectory of diamagnetic particles in ferrofluid flows in response to magnetic field gradients. The instantaneous position of a particle, $\mathbf{r}_p$, was obtained by integrating the particle velocity over time, written as

$$\mathbf{r}_p = \mathbf{r}_0 + \int_0^t \left[\mathbf{U}_f(t') + \mathbf{U}_m(t')\right] dt' \qquad \text{(Eq. 4-13)}$$

where $\mathbf{r}_0$ is the initial location of the particle, and t is the time coordinate. Note that both the fluid velocity, $\mathbf{U}_f$, and the magnetophoretic particle velocity, $\mathbf{U}_m$, are dependent on position, and so vary with time during the particle migration. This work excluded the contributions of gravity and inertia in the particle velocity in Eq. 4-13. As per the

manufacturers, the mass densities of the original EMG 408 ferrofluid and the diamagnetic particles are 1.07×10^3 kg/m^3 and 1.05×10^3 kg/m^3, respectively, which yields a net gravity-buoyancy force of 1.28×10^{-2} pN for 5 μm-diameter particles. This force is two orders of magnitude smaller than the magnetic force illustrated in Fig. 4-3, and can cause particle sedimentation at a speed of 0.27 μm/s at most. Hence, the gravity effects are not considered. In addition, the largest flow rate in the experiment is 960 μL/hr, equivalent to an average flow speed of 19.2 mm/s. Hence, the calculated particle Reynolds number is only 0.024 for the biggest 10 μm-diameter particles used. This is at least 20 times smaller than the value reported at which the cross-stream inertial particle motion is observed [68]. Therefore, particle inertia is also neglected in this analytical model.

A custom-written Matlab® program was used to determine the particle position, $\mathbf{r}_p$, with respect to time and to plot the particle trajectory. In total, 20×10 (in the form of width×depth) evenly distributed points were picked at the entrance of the microchannel as the initial particle positions. The integral of particle velocity over time in Eq. 4-13 was implemented by summing the products of the particle velocity and the time step length at each time step. A sufficiently small time step (0.1 ms) was chosen to ensure the accuracy of the computation. All parameters involved in the 3D model are listed in Table 1 unless otherwise stated in the Results section.

4.4. Results and Discussion

4.4.1. Confirmation of Three-dimensional Magnetic Deflection

To confirm the three-dimensional deflection of diamagnetic particles in ferrofluid flows, this work examined the particle motions with and without a permanent magnet on-chip in both the horizontal (i.e., top view, more accurately, bottom view through an inverted microscope) and vertical (i.e., side view) planes of the microchannel. In the experiment 5 μm particles were re-suspended in 0.5× EMG 408 ferrofluid (i.e., the original ferrofluid was diluted to its half concentration with pure water). A permanent magnet was either placed 2.2 mm away from the microchannel (ΔL = 2.2 mm in Fig. 4-1b) 2 mm upstream of the prism or removed from the microfluidic chip.

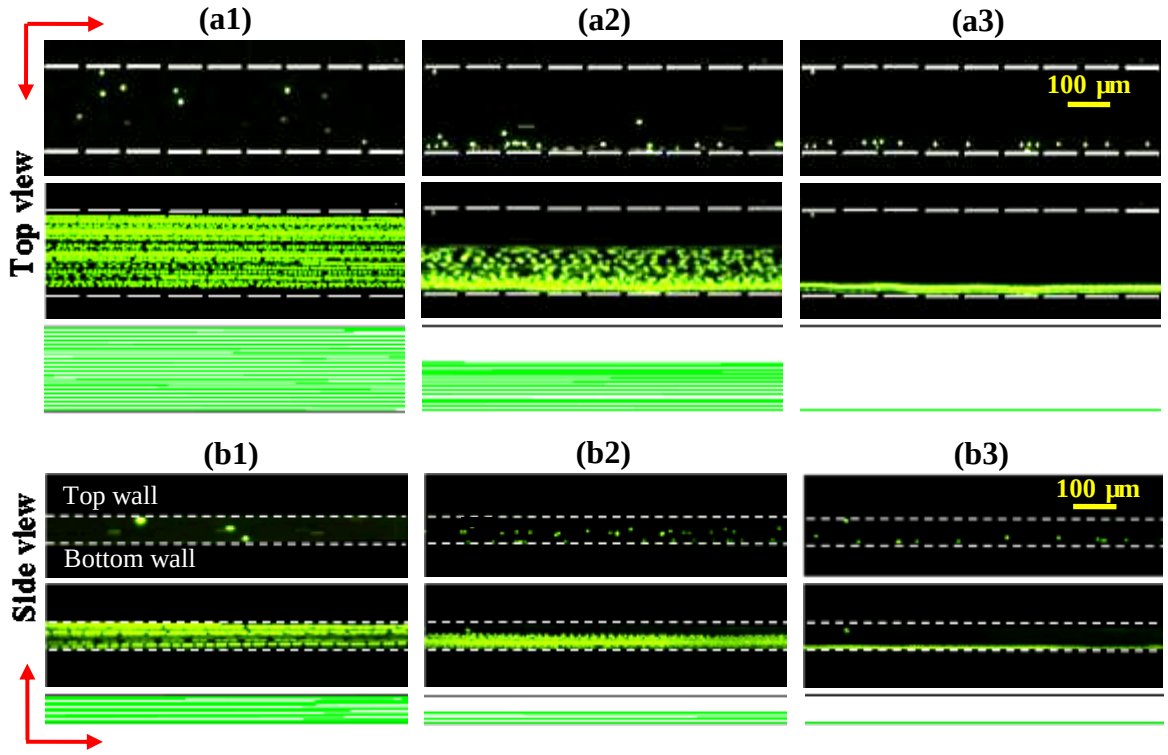

Fig. 4-4: Demonstration of the three-dimensional deflection of 5 μm diamagnetic particles in 0.5× EMG 408 ferrofluid for the cases of without magnet (a1, b1) and with magnet at the flow rate of 180 μL/hr (a2, b2, equivalent to an average flow speed of 3.6 m/s) and 45 μL/hr (a3, b3). The top, middle, and bottom rows in each panel demonstrate the snapshot image, superimposed image, and theoretically predicted trajectories of 5 μm particles, respectively.

Fig. 4-4 compares the experimentally obtained snapshot (top row) and superimposed (middle row) images with the theoretically predicted particle trajectories (bottom row) for both the top (a1-a3) and side (b1-b3) views. In the absence of the magnet, particles simply follow the *x*-direction ferrofluid flow and cover the channel cross-section uniformly for the flow rates tested. This is evidenced by the experimental images in Fig. 4-4 (a1, b1), which are indicated by the predicted particle trajectories in both view planes. However, when the magnet is on-chip, particles can only partially

cover the width and depth of the channel due to magnetic deflection. Moreover, as expected, this deflection decreases with increasing flow rate in both directions as demonstrated in Fig. 4-4 (a2, a3, b2, b3). This work finds that with a flow rate of 180 μL/hr (equivalent to an average flow speed of 3.6 mm/s), particles deplete in the half of the channel width [Fig. 4-4(a2)] and depth [Fig. 4-4(b2)] closer to the magnet center. In contrast, particles are deflected fully in both the width and depth directions at a reduced flow rate of 45 μL/hr, and focused to a single file in the outer bottom corner of the microchannel (see (a3) and (b3) in Fig. 4-4), the farthest from the center of the magnet. These experimental observations match the theoretical predictions qualitatively. A quantitative study of the factors that affect the diamagnetic particle deflection in ferrofluid microchannel flows is presented in the following section.

4.4.2. Evolution of Particle Deflection

To understand how the magnetic deflection evolves when particles approach and move past the permanent magnet, this work studied 5 μm particle motions in 0.5× EMG 408 ferrofluid in a row of five observation windows along the channel length with reference to the position of the magnet: 2.5 mm upstream (Window 1), right before (Window 2), center (Window 3), right after (Window 4), and 2 mm downstream (Window 5). The relative positions of these observation windows to the magnet can also be read from the *x*-coordinate values in Fig. 4-5b. The magnet was placed 1.33 mm from the microchannel, and this distance was fixed in the rest of the experiments presented

below. Top-view images were taken to investigate the diamagnetic particle deflection in the horizontal direction of the microchannel only.

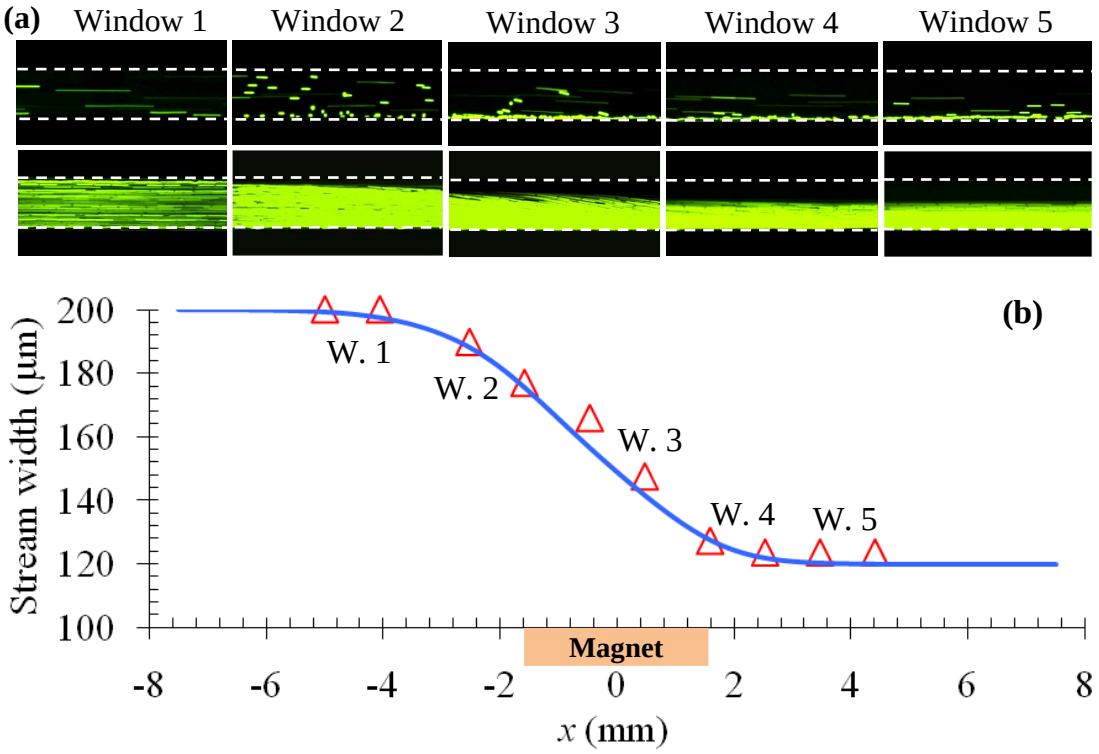

Fig. 4-5: Lengthwise evolution of the diamagnetic deflection of 5 μm particles in 0.5× EMG 408 ferrofluid at a flow rate of 480 μL/hr (equivalent to an average flow speed of 9.6 mm/s): top-view snapshot (top row) and superimposed (bottom row) images in five consecutive observation windows along the channel length (a); comparison of the experimentally measured (symbols) and theoretically predicted (curve) widths of the particle stream along the floe direction (b). The relative positions of the five observation windows (labeled as W.1-W.5) to the permanent magnet can be read from their *x*-coordinate values in (b).

Fig. 4-5a shows the top-view images in the five observation windows at a flow rate of 480 μL/hr. One can see that particles follow the fluid flow in Window 1 without

noticeable deviations, but acquire an apparent deflection in Window 2 when approaching the magnet. This magnetic deflection grows continuously to about one half of the channel width as particles move through the magnet region, which is clearly demonstrated by the images from Windows 3 and 4. It vanishes when particles move into Window 5. This trend can be explained by the axial variations of the magnetic force, $F_{m,z}$, as shown in Fig. 4-3. The data finds that the acquired diamagnetic particle deflection in Fig. 4-5a (Window 5) is comparable to that in Fig. 4-4(a2) while at a much larger flow rate. This is attributed to the stronger magnetic field and field gradients within the channel in the former situation as a result of the smaller magnet-channel distance. A quantitative comparison between the experimentally measured (symbols) and theoretical predicted (curve) widths of the focused particle stream is shown in Fig. 4-5b. A good agreement is obtained for the results in all five observation windows.

4.4.3. Effect of Flow Rate

As demonstrated in Fig. 4-4 (a2, a3, b2, b3), the diamagnetic particle deflection diminishes with increasing flow rate. A more detailed study of this flow effect is given in Fig. 4-6. Three flow rates (Q = 240, 480, and 960 μL/hr, symbols, see also the insets for superimposed top-view images) were tested for 5 μm particle suspension in 0.5× EMG 408 ferrofluid, and the obtained widths of the particle streams in Window 5 (i.e., 2 mm after the magnet, see Fig. 4-5) were compared to the theoretically predicted curve. This work finds that particles can be fully deflected when the flow rate is 240 μL/hr or less, and the eventual width of the particle stream can be reduced to the particle diameter in

principle. This and as well the particle stream widths at 480 and 960 μL/hr are predicted with good agreement by the analytical model. As indicated in Eq. 4-8, the particle *deflection* (i.e., channel width minus the particle stream width) should be inversely proportional to the flow rate if the fluid velocity is much greater than the axial magnetophoretic particle velocity. This condition is fulfilled as the induced magnetic velocity is on the order of 100 μm/s while the lowest flow velocity used in this experiment is 4.8 mm/s (for 240 μL/hr). The relationship between the particle stream width and the inverse of the flow rate is shown in the inset graph of Fig. 4-6, which is indeed approximately linear as expected. The deviation is likely associated with the three-dimensional magnetic deflection and the non-uniform fluid velocity over the channel cross-section.

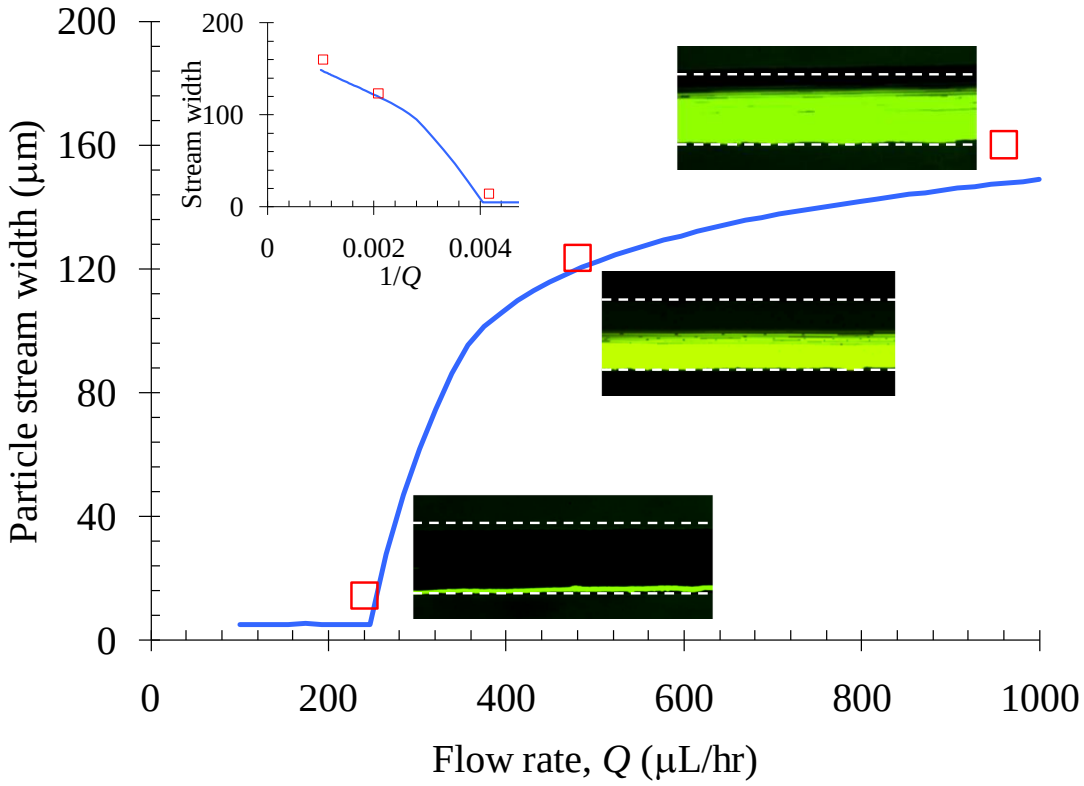

Fig. 4-6: Flow rate effect on the horizontal deflection of 5 μm diamagnetic particles in 0.5× EMG 408 ferrofluid. The symbols represent the experimental data of particle stream width measured from the corresponding top-view superimposed images. The curve is obtained from the 3D analytical model. The inset graph shows the particle stream width vs. the inverse of the flow rate.

4.4.4. Effect of Particle Size

Eq. 4-10 indicates that the induced magnetophoretic velocity is proportional to a particle diameter squared. As a result, the magnetic deflection should be a quadratic function of particle diameter if the fluid velocity is much greater than the axial magnetophoretic particle velocity. In order to verify this size effect, this research tested the magnetic deflection of diamagnetic particles of three different diameters, 2.2, 5 and 10 μm, in 0.5× EMG 408 ferrofluid at a flow rate of 480 μL/hr. Fig. 4-7 compares the

experimental data (symbols and top-view snapshot images) with the theoretical curve for the stream width of particles of different diameters 2 mm after the magnet. Note that the horizontal axis is the particle diameter squared. For 2.2 µm and 5 µm particles, the agreement is good and the particle stream width approximately scales with the square of the particle diameter. For particles larger than 8 µm the model predicts a full-width deflection and the stream width becomes equal to the particle diameter. This prediction is also verified by the experimentally measured stream width of 10 µm particles as presented in the inset image with all particles aligned on the channel sidewall.

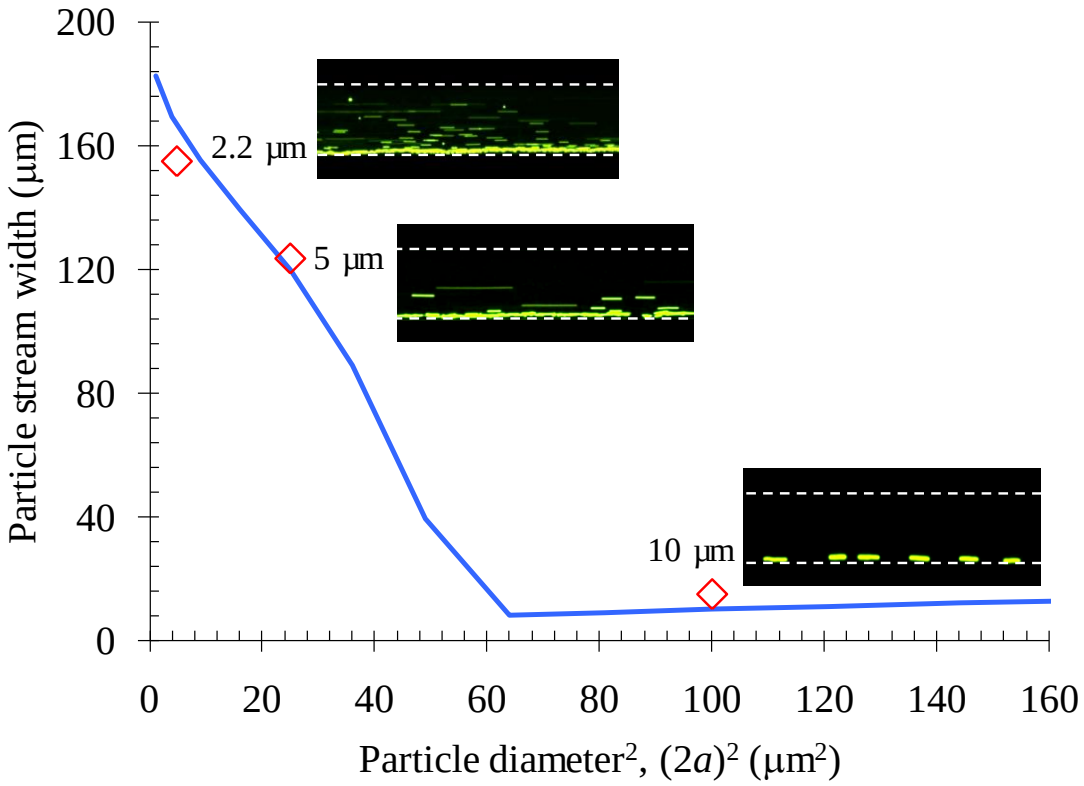

Fig. 4-7: Particle size effect on the magnetic deflection in 0.5× EMG 408 ferrofluid at a flow rate of 480 µL/hr. The symbols represent the experimental data of particle stream width measured from the corresponding top-view superimposed images (only snapshot images are exhibited). The curve is obtained from the 3D analytical model.

4.4.5. Effect of Ferrofluid Concentration

The volume concentration of magnetic nanoparticles, ϕ, affects the magnetization, $\mathbf{M}_f$, and viscosity, η, of ferrofluids, both of which are involved in Eq. 4-10 for magnetophoretic particle velocity. For simplicity this work neglects the magnetoviscous effects[69] and treats η as a linear function of ϕ via $\eta = 10^{-3} + \phi/60$ (kg/m/s), which gives η = 1.2, 1.1, and 1.05 ($\times 10^{-3}$ kg/m/s) for the original (ϕ = 1.2%), 0.5× (ϕ = 0.6%), and 0.25× (ϕ = 0.3%) EMG 408 ferrofluids, respectively. As $\mathbf{M}_f$ scales linearly with ϕ [see Eq. 4-2], which is to a greater extent than the according change in η, the diamagnetic particle deflection in ferrofluids is expected to be approximately proportional to ϕ. This analysis is verified by Fig. 4-8, where the experimentally measured stream widths of 5 μm particles in ferrofluids of the above three concentrations (symbols and the inset images) closely match the theoretical prediction (curve).

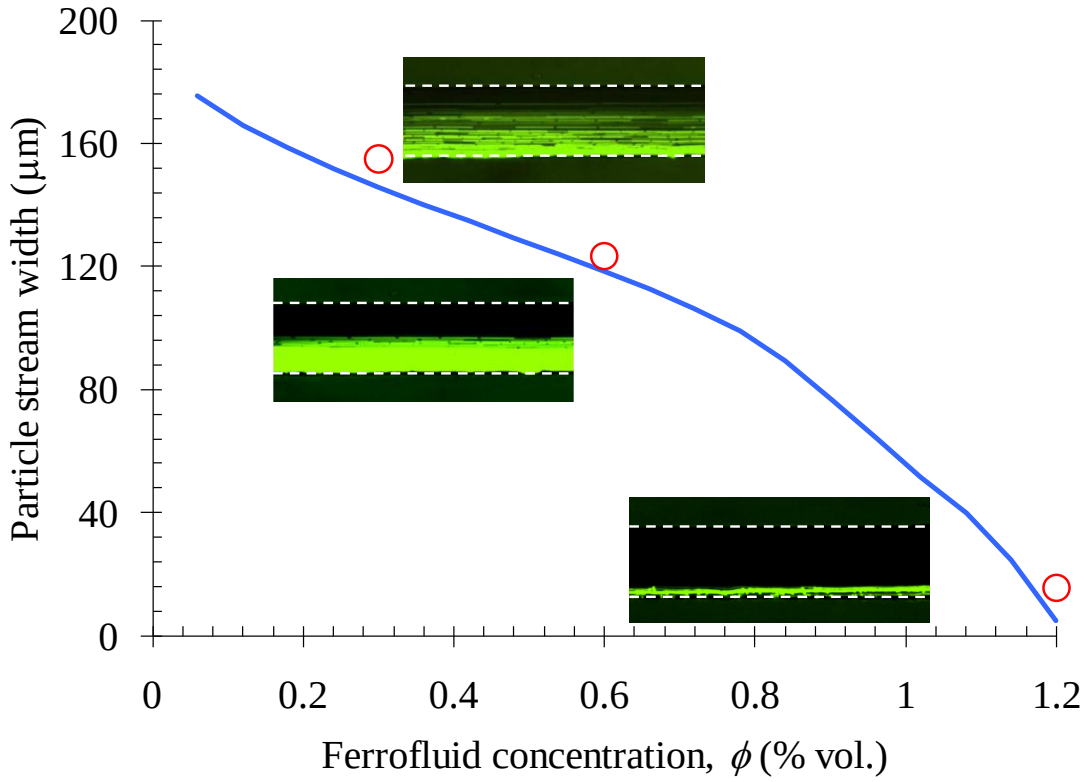

Fig. 4-8: Ferrofluid concentration (i.e., the volume fraction of magnetic nanoparticles) effect on the diamagnetic deflection of 5 μm particles at a flow rate of 480 μL/hr. The symbols represent the experimental data of particle stream width measured from the corresponding top-view superimposed images. The curve is obtained from the 3D analytical model.

4.5. Conclusions

This chapter performed a fundamental study of diamagnetic particle deflection in ferrofluid flows through a rectangular microchannel. It is found that diamagnetic particles can be deflected both outwards and downwards over the channel cross-section, forming a focused particle stream flowing near the corner that is the farthest to the center of the magnet and bears the smallest magnetic field. This three-dimensional deflection grows as

particles approach and move past the magnet, where the effective range is within about a 2 mm distance before and after the magnet in the experiment. The eventual particle deflection in the channel width direction was observed to increase with the decrease of flow rate or the increase of ferrofluid concentration and particle size. This work also developed a three-dimensional analytical model to understand and simulate the diamagnetic particle deflection in ferrofluid flows. The theoretical predictions agree with the experimental results quantitatively. It is anticipated that the demonstrated particle deflection in the horizontal and vertical planes of the microchannel may be exploited to realize a three-dimensional focusing of cells for microflow cytometry applications.

CHAPTER 5 : PARTICLE FOCUSING BY MAGNETOPHORETIC METHOD

5.1. Background on Magnetic Focusing

As proven from the fundamental study for diamagnetic particle deflection using *negative* magnetophoresis, the magnetic method is also found capable of supplying sufficient deflection efficiency and accuracy. More importantly, the large throughput and the continuous working mode just add another two important attributes to this processing method. It is believed with minor adjustments to the microchannel designs that the magnetophoresis phenomenon can be utilized to realize particle focusing and many other advanced particle controls.

As mentioned in Chapter 3, numerous physics fields have been applied to achieve particle focusing. Only recently has magnetic field been exploited to focus particles in microfluidic devices. As compared to other techniques, magnetic method is non-invasive and free of fluid heating issues (if permanent magnets are used) that accompany nearly all other forces, and is therefore well suited to handle bioparticles [70],[71], [72]. Afshar *et al.* [73] demonstrated a three-dimensional focusing of superparamagnetic particles by the use of a pair of asymmetrically arranged electromagnetic tips. The magnetic particles are first retained on one sidewall and then progressively released by lowering the current of an electromagnetic coil. The particle focusing is then realized by introducing a sheath flow to push the particles to the channel center.

The focusing of diamagnetic particles has been obtained in paramagnetic solutions by Pamme's group [58], [74] and in ferrofluids by Mao's group[75]. In both cases

two repulsive magnets are used to create a magnetic field gradient null in the center of the microchannel that causes two difficulties in the operation. The first difficulty is to overcome the repulsion force and place the two magnets close enough to produce a large magnetic field with gradients in between. The second difficulty is to align the two magnets and keep them symmetric about the microchannel for controlling the position of the focused particle stream. To resolve these issues, Pamme's group [74], [76] used a mechanical setup to precisely align two facing magnets for a fused silica capillary. This method is unsuitable for integration into planar lab-on-a-chip devices. Zhu *et al.* [75] embedded two long magnets into PDMS for an on-chip focusing, but the distance between them was 7 mm. The result is a poorly focused stream (about 100 μm wide) of 5 μm particles. Moreover, as the tested ferrofluid is opaque, fluorescent particles must be used for visualization in the experiment [75].

In this chapter, works is presented on the development of a new approach to three-dimensional focusing of nonmagnetic particles in ferrofluid microflow using only a single permanent magnet. Since the magnet is embedded near the microchannel, the ferrofluid can be sufficiently diluted, enabling a bright-field view of the focused particles in both the horizontal and the vertical planes. As such, fluorescent labeling of the suspended particles is not required. The effects of ferrofluid flow rate and particle size on the particle focusing performance are examined.

5.2. Experiment

Fig. 5-1a presents a picture of the microchannel used in this experiment. The T-shaped microchannel was fabricated in PDMS using a modified soft lithography technique. A permanent magnet and a right-angle prism were embedded into PDMS and placed close to the microchannel for an enhanced magnetic field and the side-viewing of the particle motion, respectively. The microchannel consists of one 400 μm wide main-branch and two 200 μm wide side-branches with a uniform depth of 40 μm. Each branch is 10 mm long. The neodymium (NdFeB) permanent magnet (B221, K&J Magnetics Inc.) is 600 μm away from the main-branch (edge to edge distance) and 3 mm from the side-branch. It has a dimension of 1/8"×1/8"×1/16" (thick) with the magnetization direction being perpendicular to the main-branch. The prism (N-BK7, Edmund Optics Inc.) is 500 μm away from the main-branch and 1 mm behind the magnet along the flow direction.

Fluorescent polystyrene particles (Duke Scientific Corp.) of 5 and 10 μm in diameter were re-suspended in 0.01× EMG 408 ferrofluid (Ferrotec Corp.) to a final concentration of 10^6–10^7 particles/ml. The dilution was prepared by mixing the original ferrofluid (1.2% in volume magnetic nanoparticles) with a water-glycerol solution at a ratio of 1:99 in volume. The water-glycerol solution was prepared at the volume ratio of 7.8:2.2 in order to match the density of polystyrene particles (1.05 g/cm^3). To drive the particulate and sheath flows, two identical pipette tips were inserted into the PDMS slab serving as the inlet reservoirs. The outlet reservoir was emptied prior to the experiment. As labeled in Fig. 5-1a, the particle solution in ferrofluid was introduced to the inlet reservoir closest to the magnet (i.e., on the same side as the magnet with respect to the

main-branch). Meanwhile, an equal volume of water-glycerol solution (also 7.8:2.2 in volume to closely match the viscosity and density of the particle-suspending ferrofluid) was injected into the other inlet reservoir to obtain an identical flow rate in the two side-branches.

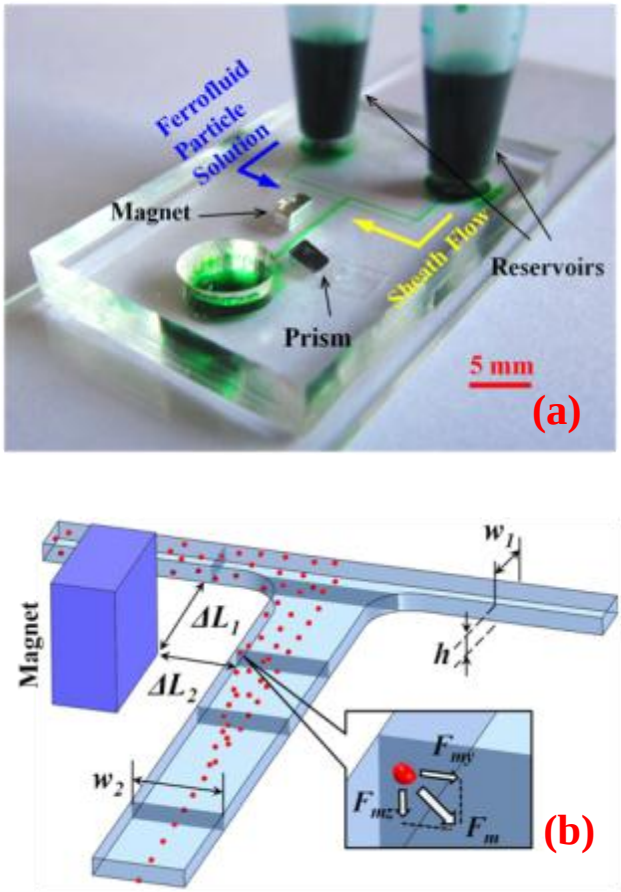

Fig. 5-1: Picture of the microfluidic device used in the experiment (a), and schematic of the magnet-microchannel system (b).

5.3. Theory

5.3.1. Mechanism for diamagnetic particle focusing

Nonmagnetic particles experience a negative magnetophoretic force, $\mathbf{F}_m$, in ferrofluid when subjected to a non-uniform magnetic field, and for small particles this force is given in Eq. 4-1:

$$\mathbf{F}_m = -V_p \mu_0 \left(\mathbf{M}_f \bullet \nabla\right)\mathbf{H} \qquad \text{(Eq. 4-1)}$$

This force exists only when the particles are subjected to a magnetic field gradient and the particle sizes are small enough so that the field gradient within the particle volume can be neglected. In this analysis, particle self-magnetization and demagnetization effects on the local magnetic field is neglected, since the particle susceptibility is small even compared to that of the highly diluted ferrofluids, and it is taken as a diamagnetic material.

Owing to the negative sign in Eq. 4-1, $\mathbf{F}_m$ is directed against the magnetic field gradient. Therefore, nonmagnetic particles are repelled from the magnet (more specifically, the magnet center where the magnetic field achieves the maximum) and deflected across the ferrofluid in both the channel width and depth directions as indicated by the horizontal and vertical components of $\mathbf{F}_m$ in Fig. 5-1b. Such three-dimensional diamagnetic particle deflection was demonstrated in Chapter 3 in a ferrofluid flow through a straight microchannel.

Since nonmagnetic particles experience a negligible magnetic force in water, the ultimate position of those three-dimensionally deflected particles in the main-branch of the T-microchannel is to follow the interface of the ferrofluid and sheath water in the

horizontal plane and to flow directly above the bottom channel wall in the vertical plane. This is achieved so long as sufficient residence time is available for particles to accept the diamagnetic deflection inside the ferrofluid. As the 0.01× ferrofluid used in this experiment has approximately the same density and viscosity as those of water (note that both solutions were mixed with glycerol to obtain the desired density), an equal volume of these two fluids in both inlet reservoirs is expected to produce a similar flow rate in the two side-branches. As such, the interface between the two co-flowing fluids should align with the center plane of the main-branch if diffusional mixing is considered slow and neglected. In other words, nonmagnetic particles are expected to exit the main-branch of the T-microchannel in a focused stream near the bottom edge of the center plane as schematically illustrated in Fig. 5-1b.

The effectiveness of such three-dimensional diamagnetic particle focusing is dependent on the particle deflections in both the horizontal and vertical planes, which are determined by the ratios of the particle speeds perpendicular and parallel to the flow,

$$deflection_i = \frac{U_{p,i}}{U_{p,x}} = \frac{U_{m,i}}{U_f + U_{m,x}} \approx \frac{U_{m,i}}{U_f} \qquad (i = y, z) \qquad \text{(Eq. 4-8)}$$

Balancing the magnetic force, $\mathbf{F}_m$, in Eq. 4-1 with the Stokes drag force yields the magnetophoretic particle velocity, $\mathbf{U}_m$,

$$\mathbf{U}_m = \frac{\mathbf{F}_m}{6\pi\eta a f_D} = \frac{-\mu_0 \phi a^2}{9\eta f_D} \frac{M_d L(\alpha) \nabla \mathbf{H}^2}{H} \qquad \text{(Eq. 4-10)}$$

where η is the ferrofluid viscosity, a is the radius of nonmagnetic particles, and f_D is the drag coefficient that is used to account for the particle-wall interactions. By neglecting the contribution of magnetophoresis to the x-direction particle velocity [see the

approximation in Eq. 4-8], one can see that the particle *deflection* and hence focusing increase with the rise of nonmagnetic particle size and magnetic nanoparticle concentration (i.e., the ferrofluid concentration) or with the reduction of ferrofluid speed.

5.3.2. Simulation of particle trajectory

Magnetic field was solved using an analytical model in Matlab® developed in Chapter 3. Particle trajectory was determined using the Lagrangian particle tracking method described in section 2.2.2. This occurred where evenly spaced particles at the entrance were tracked from initial positions adding cumulative products of instantaneous speed and time step and the local effective ferrofluid magnetization $\mathbf{M_f}$ was determined using Langevin function Eq. 4-1, and the transient force was calculated using Eq. 4-1. Due to the applicable limitation of cross-sectional velocity distribution in a rectangular channel, the T-junction part and other channel turns were not used in the simulation. Therefore, only the 10 mm long straight channel was used to predict the particle trajectories, since the focusing only happens in this channel. Fig. 5-2 highlights the simulation domain in the red box. And it was confirmed from the experimental observation that, the T-junction effect was small and the flows will join and become fully developed within 0.5 mm from the T-junction.

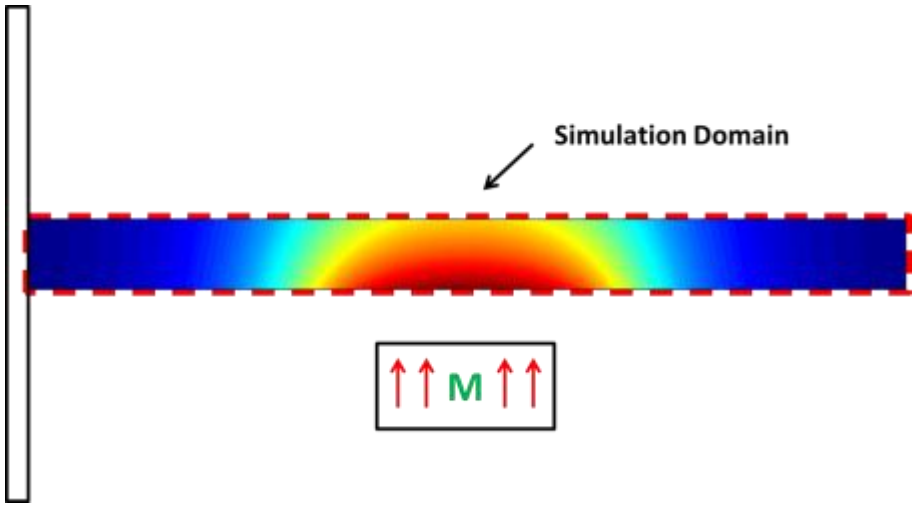

Fig. 5-2: Simulation domain for particle trajectories

Particle stream was released from the bottom half of the main channel inlet. Magnetophoretic phenomenon only applies to the bottom half of the channel, that is, whenever a particle passes the centerline during the simulation, its traverse velocity in channel width or depth direction will be assigned zero.

5.4. Results and Discussion

5.4.1. Demonstration of three-dimensional diamagnetic particle focusing

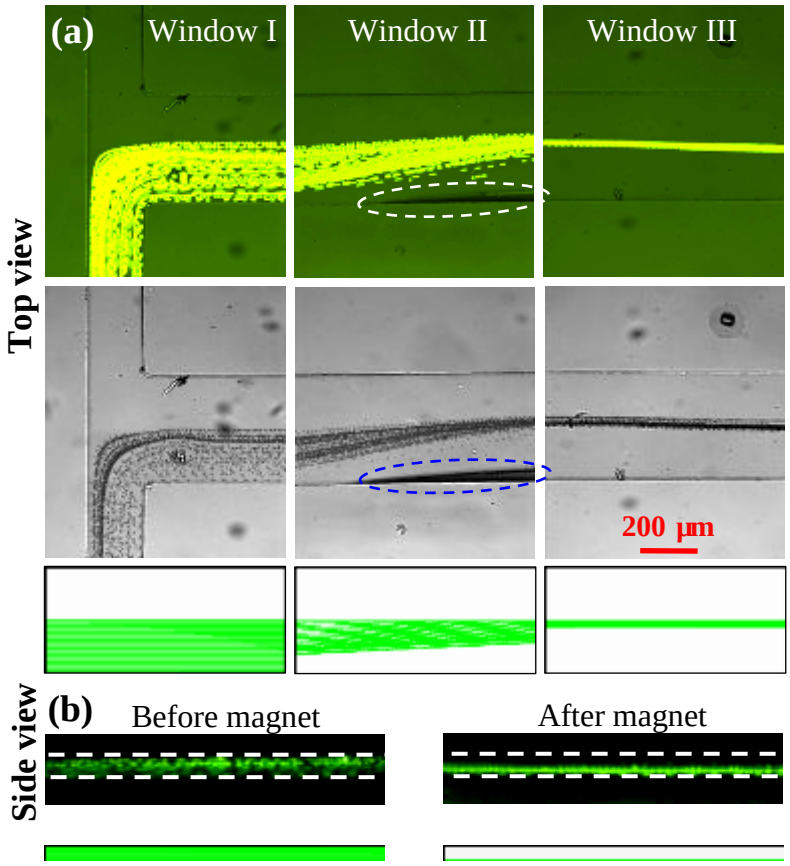

Fig. 5-3: Illustration of three-dimensional focusing of 5 μm nonmagnetic particles in ferrofluid flow through a T-microchannel using a single magnet: (a) top-view streak images (fluorescent in the top row and bright-field in the bottom row) in the three view-windows I, II and III (refer to Fig. 1(b) for the locations); (b) side-view streak images before (left) and after (right) the magnet. The mean flow speed of the ferrofluid in the side-branch is 0.5 mm/s. The dashed lines in (a) highlight the trapped magnetic nanoparticles on the sidewall that is nearer to the magnet. The scale bar in (b) represents 200 μm. Simulated particle trajectories are shown below the experiment results.

Fig. 5-3 shows the top (a) and side-view (b) images of 5 μm nonmagnetic particles at the T-junction (Window I), magnet center (Window II), and 3 mm after the magnet (Window III) of the proposed ferromicrofluidic focuser (see Fig. 5-1b for the

locations of the view windows). These images are obtained by superimposing a sequence of more than 200 snapshots and are termed streak images below. The top-view results include fluorescent (top row, with a weak background light illumination to visualize the channel edges) and bright-field (bottom row) streak images, which both clearly illustrate the particle motion. Therefore, fluorescent labeling is actually not needed for particles re-suspended in the diluted ferrofluid. The mean flow speed of the ferrofluid is 0.5 mm/s in the side-branch, and was estimated by tracking 3-5 particles each at five different locations over the width of the side-branch in the straight section and then fitting the measured particle speeds to the fluid velocity profile in a rectangular channel.

At the T-junction (see Window I in Fig. 5-3a), particles experience negligible magnetic force and thus cover uniformly one half of the main branch without noticeable deflections. When particles move past the magnet center (see Window II in Fig. 5-3a), apparent deflection toward the channel center plane is observed. However, particles are all confined by the sheath water and unable to cross the ferrofluid-water interface. A significant amount of magnetic nanoparticles accumulates at the sidewall nearest to the embedded magnet, as highlighted by the dashed-lines in the top-view images in Window II. Moreover, the accumulated nanoparticles seem to disturb the ferrofluid/water co-flows and shift their interface slightly away from the channel center plane. This phenomenon can be mitigated by the use of a larger flow rate, where particle focusing can be maintained by reducing the channel width. In addition, the instability of the ferrofluid/water interface under a magnetic field[77] may contribute to the off-center deviation of the focused particle stream as well. This issue will be investigated in future

studies. At 3 mm after the magnet (see Window III in Fig. 5-3a), 5 μm particles are focused to a less than 25 μm-wide stream flowing along the channel center plane. Note that the particle stream is 200 μm wide before the magnet, indicating a more than 8-fold focusing in the horizontal plane in terms of particle stream width.

Simulated particle trajectories are shown below the experiment results in Fig. 5-3, which shows a good agreement with the experiment result at all three observation windows. Compared to the entrance flow at Window I, it is confirmed that the two streams join smoothly and become fully developed soon afterwards.

Side-view images were recorded through an embedded prism 1 mm before or after the magnet along the flow direction. Only the fluorescent streak images are illustrated in Fig. 5-3b. It is observed that before the magnet (Fig. 5-3b, left) 5 μm particles disperse uniformly in the suspension and spread nearly the entire channel depth. Moreover, they migrate through the microchannel at significantly non-uniform speeds, implying that the particles were moving at different depth levels. In contrast, all the particles travel adjacent to the bottom channel wall and form a tight bright stream after the magnet (Fig. 5-3b, right). Furthermore, their travelling speeds become nearly identical to each other, indicating a good particle focusing in the vertical plane. Simulated particle trajectories at Window I and III for side-view are also included and validate the focusing in the depth direction.

5.4.2. Flow Rate Effect

By varying the injected ferrofluid and water volumes in the two inlet reservoirs, this work examined the flow rate effect on diamagnetic particle focusing in the T-microchannel. Fig. 5-4a compares the snapshot (left column) and streak (right column) images of 5 μm particles at the mean ferrofluid flow speed of 0.5 (top row), 1.0 (middle row), and 2.0 (bottom row) mm/s, respectively. As predicted in Eq. 4-8, increasing the ferrofluid flow speed reduces the particle focusing in the horizontal plane. Moreover, the measured particle stream width scales almost linearly with the inverse of the flow speed as demonstrated in Fig. 5-4b. This work also studied the 5 μm particle focusing in the vertical plane. A complete deflection of particles to the bottom channel wall is observed at all three flow speeds tested. This is because the deflection distance in the vertical plane (the 40 μm channel depth) is much smaller than that in the horizontal plane (200 μm half-width of the main-branch).

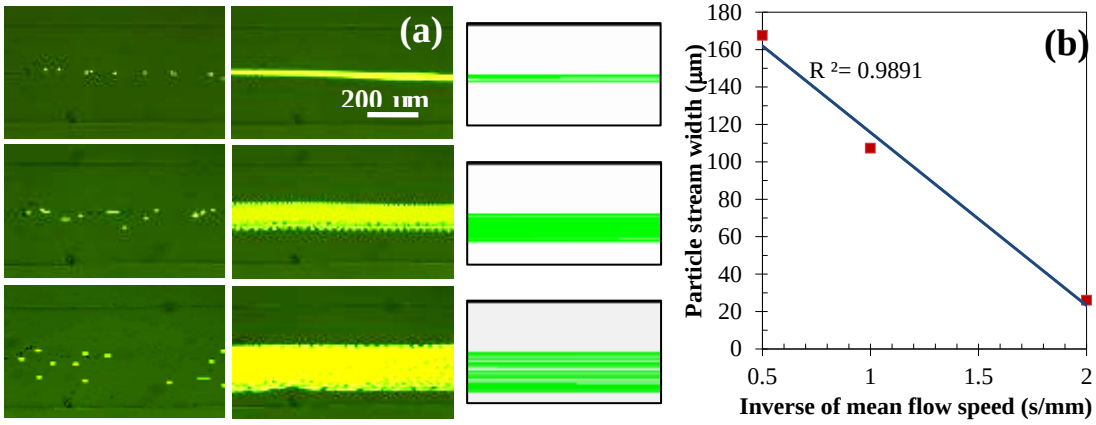

Fig. 5-4: Flow rate effect on the horizontal diamagnetic focusing of 5 μm particles in the T-microchannel: (a) snapshot images (left column) and streak (right column) images from Window III (see Fig. 1(b)) at the mean ferrofluid speed (in the side-branch) of 0.5

(top row), 1.0 (middle row), and 2.0 (bottom row) mm/s, respectively; (b) measured particle stream width (symbols) vs. the inverse of mean ferrofluid speed. The solid line in (b) is a linear fit to the experimental data with the goodness of fit indicated.

5.4.3. Particle Size Effect

Fig. 5-5 compares the horizontal and vertical focusing of 5 (a) and 10 μm (b) nonmagnetic particles in the T-microchannel through both the top and side-view images obtained in Window III. The mean ferrofluid flow speed in the side-branch is 1.0 mm/s for both cases. In the horizontal plane (see top view images in Fig. 5-5), 5 μm particles form a stream approximately 100 μm wide [refer to Fig. 5-4b]. In contrast, 10 μm particles travel through the main-branch nearly single file and form only a 20 μm wide stream along the channel centerline. This observation agrees with the quadratic dependence of magnetophoretic particle velocity on particle size as shown in Eq. 4-10. In the vertical plane (see the side-view images in Fig. 5-5), however, both 5 and 10 μm particles achieve a full-depth deflection and travel near the bottom channel wall. This is consistent with the observation in studying the flow rate effect, and is attributed to the much smaller channel depth than width.

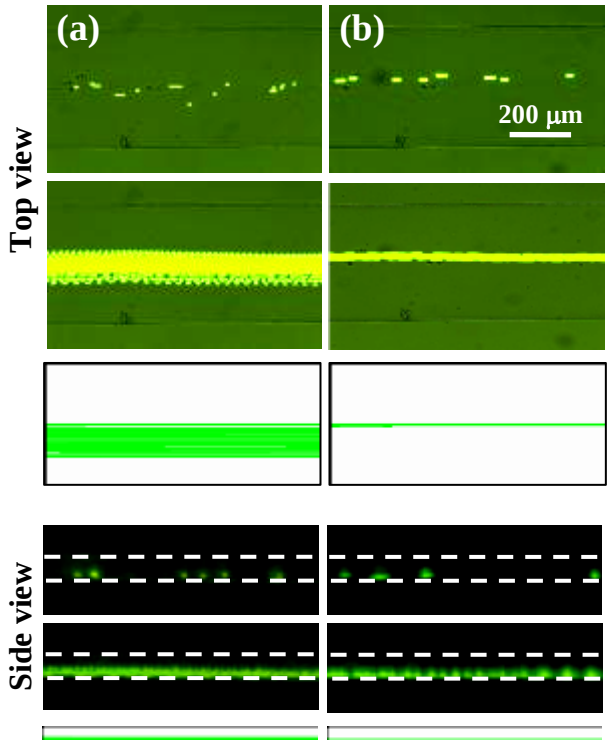

Fig. 5-5: Particle size effect on the horizontal (top view) and vertical (side view) focusing of 5 (a) and 10 μm (b) nonmagnetic particles in the T-microchannel at the mean ferrofluid flow speed of 1.0 mm/s. The top and bottom images in each panel are, respectively, the snapshot and streak images in Window III (see Fig. 1(b)). The scale bar in the top-right image represents 200 μm.

5.5. Conclusions

This chapter presented data that established a new magnetic approach to three-dimensional focusing of nonmagnetic particles using ferromicrofluidics with a single permanent magnet. This method maintained the advantages of low cost and large throughput for magnetic methods, and used a single magnet that resolved operation difficulties found in traditional magnetic focusing methods. Since ferrofluid is used to generate the magnetic "buoyant force," magnetic labeling is not needed for the suspended

particles. Moreover, as the magnet is embedded into PDMS and placed close enough to the microchannel, the ferrofluid can be diluted sufficiently to enable a direct visualization of the suspended particles in a bright field. As such, fluorescent labeling of particles is not necessary. This demonstrated that diamagnetic particle focusing has near-term applications to three-dimensional label-free (i.e., require neither magnetic nor fluorescent labeling) cellular focusing in lab-on-a-chip devices.

CHAPTER 6 : PARTICLE SEPARATION BY MAGNETOPHORETIC METHOD

6.1. Background on Magnetic Separation

Particle separation refers to isolating the different particle compositions from well-mixed samples, based on the dissimilar reactions from physics/chemical properties of each composition under the existing physical fields. Similar to the particle focusing, plenty of methods have been attempted to attain the particle separation, including electric [78], [79], acoustic [7], [80], and optical [11], [81] to name but a few. Yet, due to the non-invasive and many other inherent advantages, the magnetic technique is deemed well suited to handling biological particles [82], [71] and capable of obtaining the same control effect.

Actually, the magnetic technique has been utilized significantly to separate magnetic from diamagnetic particles or cells, relying on the distinct opposite magnetic responses of the two types of particles, namely *positive* and *negative* magnetophoresis. Miltenyi *et al.*[83] developed a MACS (magnetic cell sorter) that diverts cell mixture passing high gradient magnetic columns inside the microchannel, retaining the magnetically labeled cells and driving unlabeled cells to pass. Following that, Kantor [84] and Choi [85] presented similar methods to trap and separate magnetic particles/cells from others, using improved design and bio-sampling techniques. However, one obvious drawback of these methods is that the separation has to be conducted in a batch mode, that is, unlabeled particles/cells need to be diverted and separated completely first, and only then can magnetically labeled particles/cells be washed out after the field is removed. This essentially limits the maneuverability of particle manipulation.

Meanwhile, Inglis *et al.* [86] tried to trap magnetically labeled cells and alter their directions of flow with an array of microfabricated magnetic strips, and bypass the non-magnetically labeled cells, enabling continuous cell separation. Chalmers[87] designed two flow-through immunomagnetic cell separation devices, which also enabled continuous separation of magnetically labeled cells and unlabeled cells into multiple channel outlets. Furthermore, Adams *et al.* combined the magnetic effect with the hydrodynamic effect [88] or acoustic field [89] to enhance this magnetic and diamagnetic particle separation. Nevertheless, one common defect of these MACS systems is that, in order to obtain stable performances of the above methods, the throughput becomes a major sacrifice.

Until recently, Pamme *et al.* [90] presented a method to separate magnetic and diamagnetic particles into multiple branches according to their different responding rate on magnetophoresis. Zhu *et al.* [91] also introduced a magnetophoretic method to separate the diamagnetic particles of two different sizes. However, both methods required the input of sheath flow to pre-focus particle streams and with application of the magnetophoretic separation on this already focused particle stream this inevitably limited the throughput of the particle processing.

In this chapter, two types of separation scheme are introduced that utilize both *positive* and *negative* magnetophoresis. In the first method, a similar principle from previous MACS systems was adopted to trap magnetic particles with an external magnetic field. In contrast to the former method, the second method performed a continuous magnetic separation in ferrofluid at a relatively high flow rate, using the same

channel structure as the first method. Moreover, the same T-shaped microchannel (Fig. 5-1a) was used in these particle separations.

6.2. Experiment

PDMS microchannel was fabricated and used in this experiment (Fig. 6-1). This T-shaped microchannel was of the same geometry as the microchannel used in Chapter 4 that was 10 mm long in the straight main channel with another 10 mm long branch from the junction to outlet reservoir. It was 200 and 400 μm wide in the branch and main channels, respectively with a height (*h)* of 40 μm. The same neodymium (NdFeB) permanent magnet (B221, K&J Magnetics, Inc.) was used in this work and was positioned 500 μm from the main channel, and 3 mm from the branch (edge to edge distance), with the polarizing direction facing the main channel.

For this experiment, 3 μm magnetic particles (Bang's Lab, Inc. USA) and 10 μm diamagnetic polystyrene particles (Scientific Corp. USA) were mixed and re-suspended in two types of mediums: pure DI water and 0.1X diluted EMG 408 ferrofluids (Ferrotec Corp. USA).

The particle solution was driven through the microchannel by an infusion syringe pump (NE-300, New Era Pump Systems, Inc., NY), and Teflon tubing (1622L, Upchurch Scientific) was used to connect the microchannel and the pump. During the experiment, the fluids in the outlet reservoirs were emptied regularly to prevent buildup flow resistance.

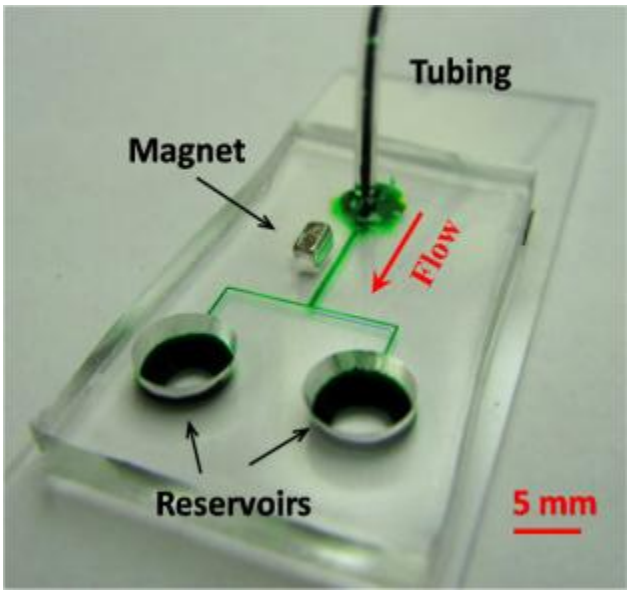

Fig. 6-1: Experiment setup.

6.3. Theory

6.3.1. Mechanism of particle separation

In magnetic particle manipulation, magnetophoresis is a key phenomenon that utilizes the difference of the magnetic properties and response between the particle and surrounding medium. It is stated that for both *positive* and *negative* magnetophoresis, the magnetic buoyancy force acting on the small particles can be given as[58]:

$$\mathbf{F}_m = V_p \mu_0 \left(\left(\mathbf{M}_p - \mathbf{M}_f \right) \bullet \nabla \right) \mathbf{H} \qquad \text{(Eq. 6-1)}$$

where V_p is the volume of the particle, $\mu_0 = 4\pi \times 10^{-7}$ H/m is the permeability of free space, $\mathbf{M}_p$ and $\mathbf{M}_f$ are the effective magnetization of the particle and ferrofluid, respectively, and $\mathbf{H}$ is the magnetic field at the particle center. It is determined by the sign of the subtraction of ($\mathbf{M}_p$ - $\mathbf{M}_f$) that the magnetophoretic force is either pushing or repelling the particle along the magnetic field increasing direction, namely *positive* or *negative*

magnetophoresis. After expanding Eq. 6-1, it can be seen more clearly from the two terms that the magnetophoretic force results from the magnetization of the particle and the ferrofluild:

$$\mathbf{F}_m = V_p \mu_0 \left(\mathbf{M}_p \bullet \nabla\right)\mathbf{H} - V_p \mu_0 \left(\mathbf{M}_f \bullet \nabla\right)\mathbf{H} \qquad \text{(Eq. 6-2)}$$

For *positive* magnetophoresis, the highly susceptible magnetic particle will generate an opposing magnetic field in response to the external magnetic field. To consider the particle self-demagnetization effect, the inside particle magnetic field $\mathbf{H}_{in}$ is used to determine the magnetic particle magnetization $\mathbf{M}_p$, rather than the applied magnetic field at particle center $\mathbf{H}$[66],[92]:

$$\mathbf{M}_p = x_p \mathbf{H}_{in} \qquad \text{(Eq. 6-3)}$$

where χ_p is the volume susceptibility, and $\mathbf{H}_{in} = \mathbf{H} - \mathbf{H}_{demag}$, and usually $\mathbf{H}_{demag} = \mathbf{M}_p / 3$ is the self-demagnetization field in the particle. Therefore,

$$\mathbf{H}_{in} = \frac{\mathbf{H}}{1 + x_p / 3} \qquad \text{(Eq. 6-4)}$$

$$\mathbf{M}_p = \frac{x_p}{1 + x_p / 3}\mathbf{H} \qquad \text{(Eq. 6-5)}$$

After taking $\mathbf{M}_p$ and $\mathbf{H}_{in}$ back to Eq. 6-2, the calculations will obtain the magnetic force for the magnetic particle in *positive* magnetophoresis:

$$\mathbf{F}_m = V_p \mu_0 \frac{x_p}{1 + x_p / 3}\left(\mathbf{H} \bullet \nabla\right)\mathbf{H} - V_p \mu_0 \left(\mathbf{M}_f \bullet \nabla\right)\mathbf{H} \qquad \text{(Eq. 6-6)}$$

On the other side, for *negative* magnetophoresis, the diamagnetic particle is considered as highly non-susceptible material so that its magnetization $\mathbf{M}_p$ is usually negligible compared to the ferrofluid magnetization $\mathbf{M}_f$. Therefore, for *negative*

magnetophoresis, the first term in Eq. 6-2 can be dropped, leaving the magnetic force for the diamagnetic particle as:

$$\mathbf{F}_m = -V_p \mu_0 \left(\mathbf{M}_f \bullet \nabla\right)\mathbf{H} \qquad \text{(Eq. 4-1)}$$

For both cases, the fluid magnetization $\mathbf{M}_f$ is calculated using the Langevin function and applied magnetic field at particle center **H**, in Eq. 4-2 and Eq. 4-3.

In this experiment, particle mixtures were introduced from the inlet tubing, and particles entered the main channel randomly spaced throughout the channel cross-section. It was proven that the flow was developed fully before any magnetic interactions were performed. As the particle flow approached the magnet, a strong magnetic field and gradient were experienced by the particles, giving rise to the particle magnetophoretic motions. While flowing with the fluids in channel length direction, the particles would endure the magnetophoretic forces along the magnetic polar direction across the stream[91]. The magnetophoretic forces were different in nature and magnitude for unique types of particles, resulting in two diverse particle streams.

Two sets of separation scheme were introduced in the experiment. In the former, polystyrene and magnetic particles were suspended in DI water, which has volume susceptibility on the same order of that of polystyrene particles (referred as diamagnetic particles below). Both were deemed to be diamagnetic materials. In this case, no significant magnetophoretic forces were applied to diamagnetic particles even those exposed to strong magnetic field gradients. On the other hand, remarkable attraction motions were observed for magnetic particles, as distinct differences existed between the susceptibilities of DI water and magnetic particles. The attraction motion was too intense

that even escalated to trapping phenomenon for magnetic particles under moderate flow rates. The trapping phenomenon occurred in the channel section near the center of the magnet. Below a certain flow rate, full trapping for magnetic particles was obtained, while leaving the diamagnetic particle trajectories unaltered. In such cases, pure diamagnetic particles in DI water solution were collected at both outlet reservoirs, resulting in the separation using *positive* magnetophoresis (Fig. 6-2a).

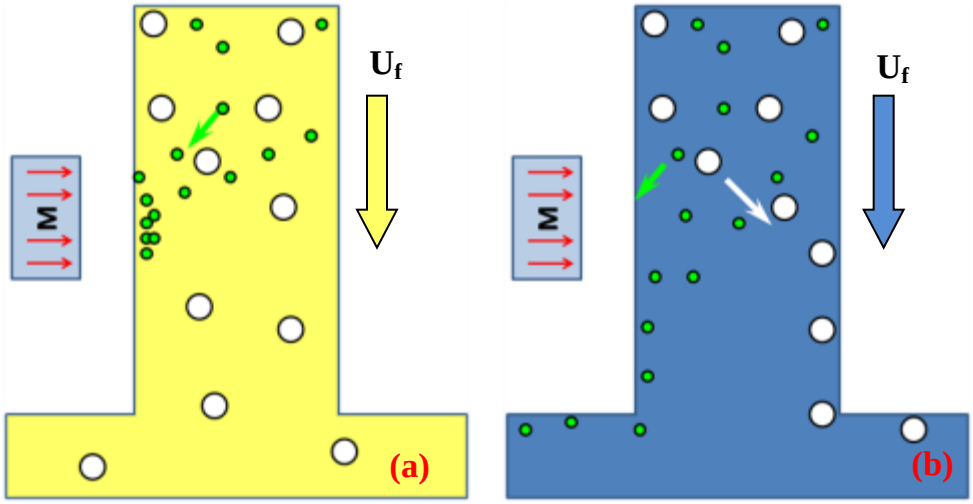

Fig. 6-2: Mechanism for the particle separation: (a) particles are suspended in DI water; (b) particles are suspended in 0.1X ferrofluid.

Fig. 6-2b demonstrates the mechanism for second separation scheme. The magnetic and diamagnetic particles were suspended in 0.1X ferrofluid. For such concentration of ferrofluids, it is sufficient to provide a susceptibility difference for the diamagnetic particles, but still incompetence to balance the magnetic particles. In this way, ferrofluids were diluted in a way that allowed the susceptibility to fall in between

the diamagnetic and magnetic particles, giving rise to *negative* and *positive* magnetophoretic phenomena simultaneously. Accordingly, as the particle stream approached the magnet region, attraction and deflection motions were developed while flowing in the main channel direction, forming two diverse particle streams moving along both sides of the channel walls. With finely tuning the flow rate, full separation can be achieved as magnetic particles flowing into the left branch and diamagnetic particles repelled into the right branch.

In addition to the width-wise separation obtained in these two schemes, the depth-wise behaviors of the particles were observed. As the magnet lie on the same vertical plane with the channel bottom, the magnet center was in fact above the channel center plane, resulting in magnetic field decreasing along the channel depth direction. Therefore, magnetic particles would move towards the channel top plane favoring the magnetic field increasing, and diamagnetic particles moved towards the channel bottom plane opposing the magnetic field increasing. From the top-view of the microscope, these vertical movements were distinguished by their change in clearness and fluorescence.

6.3.2. Simulation

Same method and channel from Chapter 4 was used for solving the magnetic field and plotting the particle trajectories. Eq. 6-6 and Eq. 4-1 were used in the Lagrangian particle tracking method described in section 2.2.2, for magnetic and diamagnetic particles, respectively. Both types of particles were released from the main channel entrance and trajectories were predicted by adding up the integration of transient velocity

with respect to time. In this simulation, magnetic particle volume susceptibility χ_p = 0.0234 was interpolated from the magnetization data curve in high **H** field, provided by the magnetic particle manufacturer [The magnetic field **H** inside the microchannel is ~$O(10^5$ A/m)].

Again, only the straight main channel was solved for magnetic field and particle trajectories and the entrance and T-junction effect did not affect the main separation inside the channel. The values used in the simulation are summarized in Table 2.

For each separation method, the flow rate required for separation needs to be accurately determined based on the magnet, particle and flow properties. The attraction or deflection rate of the particles exists in the ratio between particle velocity in main flow direction $U_{p,x}$ (x direction is the flow direction) and particle velocity in transverse directions $U_{p,i}$:

$$deflection_i = \frac{U_{p,i}}{U_{p,x}} = \frac{U_{m,i}}{U_f + U_{m,x}} \approx \frac{U_{m,i}}{U_f} \qquad (i = y, z) \qquad \text{(Eq. 4-8)}$$

In the case where magnetic-induced velocity in the main flow direction $U_{m,x}$ is trivial and in contrast with the particle flow velocity U_f, this rate only depends on the ratio of the magnetic-induced velocities in transverse directions and the flow velocity in Eq. 4-8.

The magnetophoretic particle velocity can be determined by balancing the magnetic force, $\mathbf{F}_m$ with the Stokes drag force yields, $\mathbf{U}_m = \mathbf{F}_m / 6\pi\eta a f_D$. The magnetophoretic forces in Eq. 6-6 and Eq. 4-1 are approximately proportional to the particle size cubic order a^3, and the rate can be determined by varying the flow velocity U_f, particle size a, and the magnetic field **H** as well as its gradient. Therefore when the

magnet position is fixed, the magnetic field strength and gradient will be determined, thus reducing the flow velocity U_f or increasing the particle size a to enhance the separation effect.

Table 2: List of the parameters used in the analytical model. Some of the parameters are varied in the experiment, and their specific values are referred to the text.

Parameter		**Description**	**Value**	**Unit**
Magnet	M_s	Residual magnetization	1.05×10^{6}	A/m
	x_m	Half length	3.175	mm
	y_m	Half height	3.175	mm
	z_m	Half thickness	1.588	mm
	ΔL_1	Distance between the magnet and the main channel edge	500	μm
	ΔL_2	Distance between the magnet and the branch channel edge	3	mm
Ferrofluid	ϕ	Volume fraction of magnetic nanoparticles	1.20% for original	
	M_d	Saturation moment of magnetic nanoparticles	4.379×10^{5}	A/m
	d	Mean diameter of magnetic nanoparticles	10	Nm
	η	Dynamic viscosity	1.2×10^{-3} for original	Kg/m/s
Diamagnetic particles	a	Particle radius	10	μm
Magnetic particles	a	Particle radius	3	μm
	χ_p	volume susceptibility of the magnetic particle	0.0234	
Microchannel	w_c	Main Channel width	400	μm
	h_c	Channel Height	40	μm
	Q	Volume flow rate	150, 200, 230	μL/hr

6.4. Results and Discussions

6.4.1. Threshold Separation in DI Water and 0.1X Ferrofluid

As demonstrated in previous sections, the flow rate plays a critical role in determining the rate of separation for both methods. Large flow rates would not allow sufficient residence time for the transverse particle motions. Particles can only be partially attracted or deflected to the channel walls; while at some particular flow rate, full attraction or deflection can be realized, with all particles forming single particle streamline along the channel wall. When further reducing the flow rate, the attraction or deflection trend can aggravate into trapping, if the particle is small in size and too weak to escape from the magnetic and friction forces. However, if applied to ferrofluid particle solution, this trapping always accompanies the local aggregation of the ferrofluid nanoparticles thereby inducing non-uniformity in fluid viscosity, density and magnetic properties.

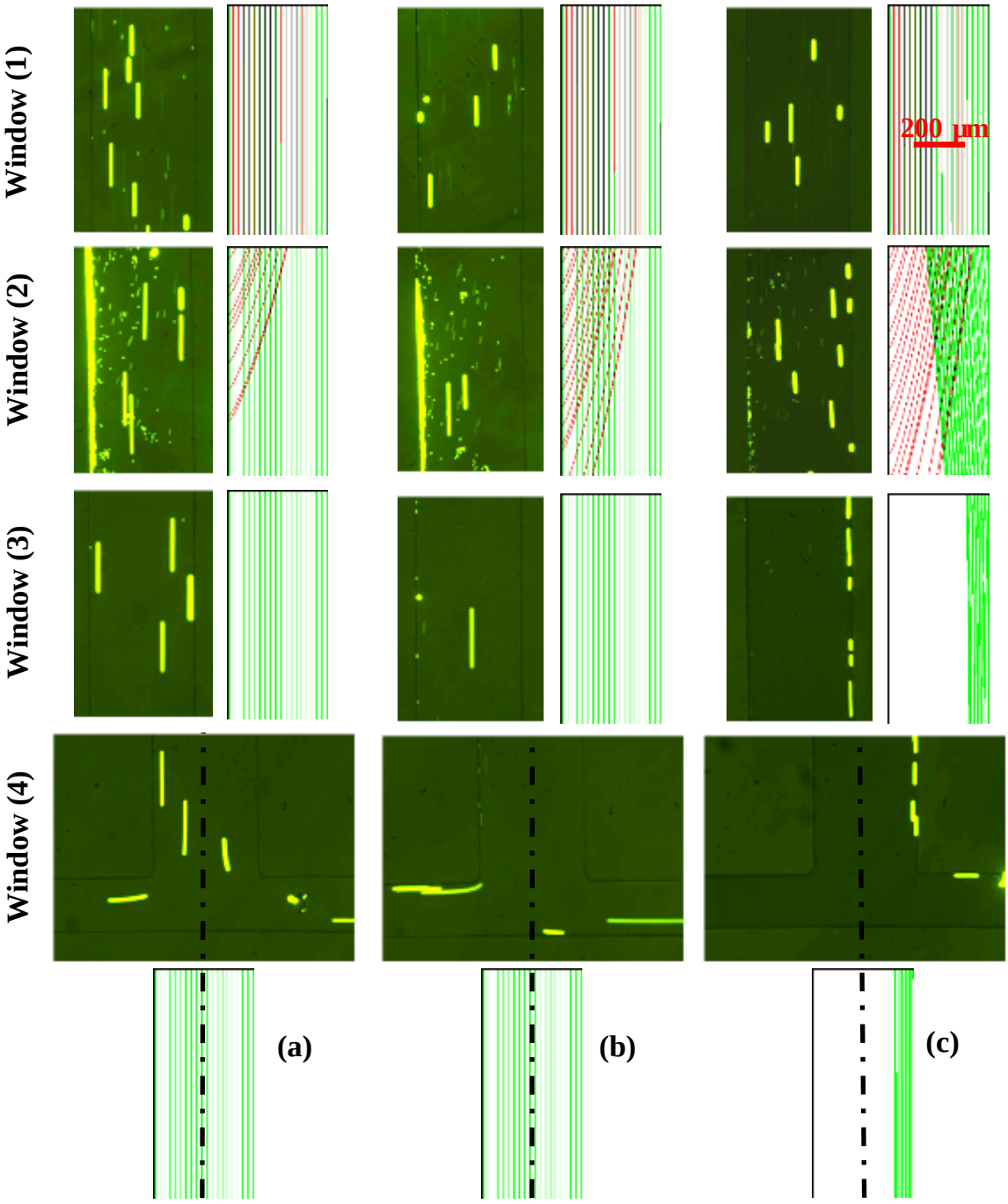

Fig. 6-3: Deflection and separation: (a) complete separation in DI water at 150 µL/hr; (b) partial passing through for magnetic particles in DI water at 200 µL/hr; (c)complete trapping for magnetic particles in 0.1X ferrofluid at 200 µL/hr. Simulation results are also included for each window sections, green and red lines represent magnetic and diamagnetic particles, respectively. Simulated particle trajectories are shown along with

the experiment results. Red and green lines denote magnetic and diamagnetic particle trajectories, respectively.

Four observation windows were used during the experiment to study the evolution process for separation at different channel sections. The four windows were chosen as: (1) 3 mm ahead of the magnet front edge where no noticeable magnetic behaviors were displayed; (2) magnet center region, where magnetic field decays fastest along its cross-channel direction; (3) magnet rear edge; and (4) T-junction region where particle streams diverge.

In Fig. 6-3, the attraction and trapping phenomena for 3 μm magnetic particles in DI water were studied at several flow rates. The simulated particle trajectories also show similar trend where red and green lines represent magnetic and diamagnetic particles, respectively. It was found that at or below the flow rate of 150 μL/hr, full trapping for magnetic particles was realized, which was equivalent to average flow speed of U_f = 2.6 mm/s in the main channel (Fig. 6-3a). As magnetic particles were smaller in size and dimmer under the same camera exposure time, their trajectories were hard to identify for fast traveling particles (see Window (1) at 150 μL/hr). When flowing near the magnet center, Window (2), remarkable deceleration of magnetic particles was noticed indicating strong opposing magnetophoretic force in the main flow direction. As particles gradually slowed down and experienced the attracting magnetophoretic forces in width and depth directions, they became fully captured by the attraction. Experiment were run for more than 10 minutes and later magnetic particles also got trapped and formed a thin layer of particles at the nearest channel wall to the magnet. On the contrary, diamagnetic particles

hardly sensed any magnetophoretic force as they followed their initial positions with the flow. In this way, two types of particles were separated by trapping magnetic particles at the magnet center region using *positive* magnetophoresis. The critical flow rate required for separation was 150 μL/hr.

Slight increasing of the flow rate would end full trapping of the magnetic particles and those entering from the farthest end from the magnet would start to escape the attraction. If flow rate gradually increases, more magnetic particles would progressively exit from the left branch (see Fig. 6-3b). At the flow rate of 200 μL/hr, magnetic particles were partially trapped and a considerable amount of the magnetic particles escaped and exited from the left branch, while pure diamagnetic particles solution were collected from the right branch thus reducing to partial separation.

However, at the same flow rate of 200 μL/hr, magnetic particles in 0.1 X ferrofluid solutions were still held at the magnet center region, similar to the trapping that happened in DI water at 150 μL/hr. This over-critical-point trapping resulted from the local aggregation of ferrofluid nanoparticles. Even though no apparent fluid color change was noticed[93],[94], the miniature ferrofluid nanoparticles still tended to migrate and accumulate in a small scale, and interacted with the incoming attracted magnetic particles, making it more difficult for magnetic particles to escape. As in Fig. 6-3c, full trapping for magnetic particles was achieved at 200 μL/hr, meanwhile all diamagnetic particles were fully or over deflected to the other side of the channel. This suggested that the critical flow rate required for full trapping of magnetic particles in 0.1 X ferrofluid solutions is higher than that for magnetic particles in DI water, and it is anticipated that the separation

utilizing both *positive* and *negative* magnetophoresis will work for a range of flow rates even larger than 200 μL/hr.

It was found that the deflection of the diamagnetic particle in 0.1 X ferrofluid was under-predicted by the simulation results compared to the experimental observation (Fig. 6-3). This was caused by the local aggregation of the ferrofluid nano-particles at the magnet side. This aggregation occupied certain space inside the microchannel and squeezed the flow to pass through a reduced cross-section. This in-channel accumulation of magnetic materials would also have certain effects on the diamagnetic particles, in other words enhanced deflection. However, such local aggregation is by far not able to be predicted using our current analytical simulation and this reduced the deviation in the deflection effects.

6.4.2. Flow Rate Effect on Ferrofluid Separation

As proved earlier for 0.1X ferrofluid solution, the separation can be achieved by completely trapping the magnetic particles and fully deflecting the diamagnetic particles to one branch at 200 μL/hr. This proves the possibility for continuous separation at even higher flow rates by further increasing the flow rate until the magnetic or diamagnetic particle stream covers more than half of the channel width.

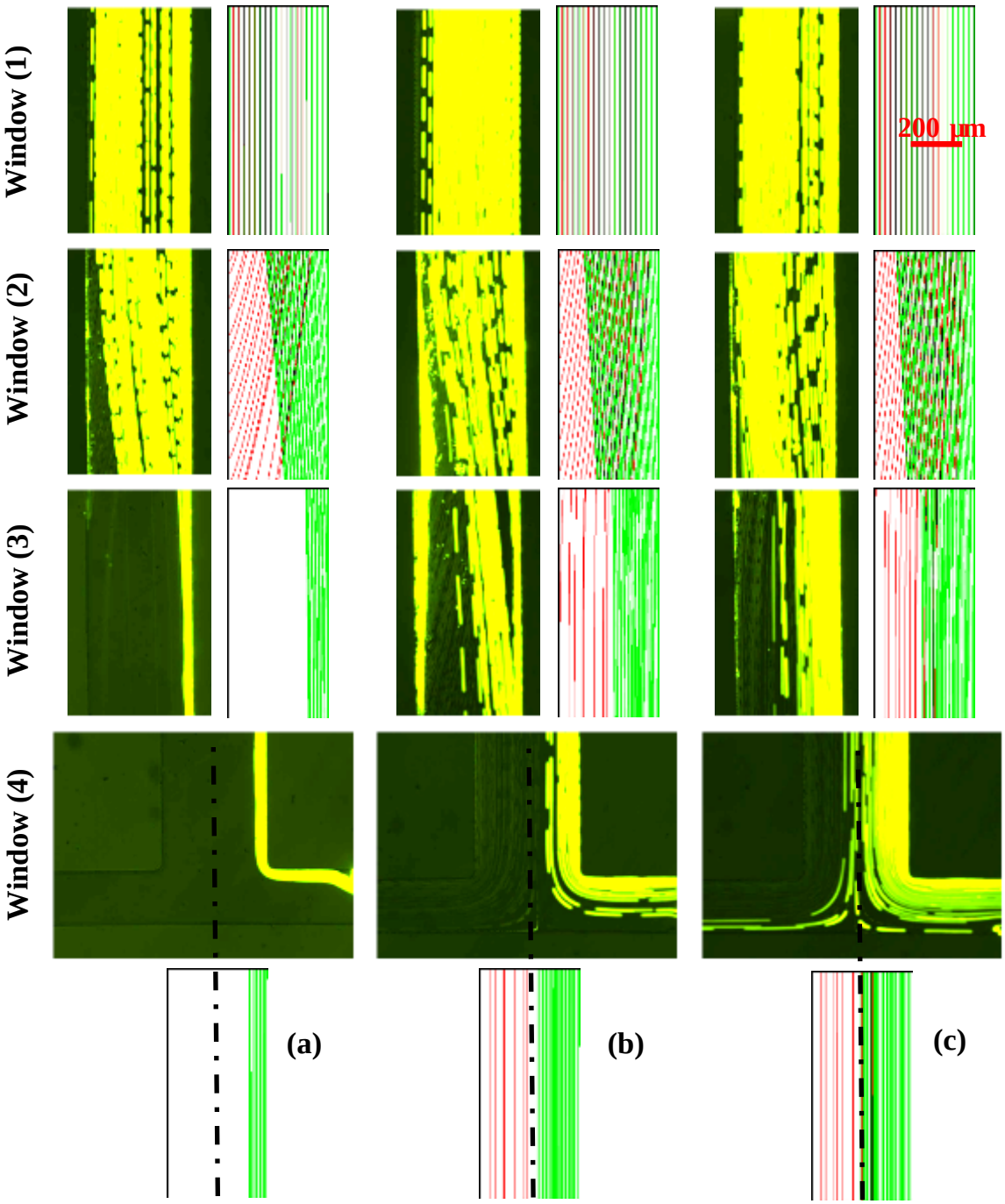

Fig. 6-4: Separation performance in different flow rates for 0.1X ferrofluid solution: (a) complete trapping for magnetic particles, 200 µL/hr; (b) continuous separation 230 µL/hr; (c) mixed separation 300 µL/hr. Simulation results are also included for each window sections, green and red lines represent magnetic and diamagnetic particles, respectively. Simulated particle trajectories are shown along with the experiment results. Red and green lines denote magnetic and diamagnetic particle trajectories, respectively.

Fig. 6-4 demonstrates this separation scheme and compares the separation rate at three different flow velocities. As described earlier, at a flow rate of 200 μL/hr, magnetic particles were fully trapped at the magnet center while diamagnetic particles were deflected to the other side, enabling separation by collecting only one type of particles at one outlet reservoir (see Fig. 6-4a).

By increasing the flow rate to 230 μL/hr, the optimal separation was obtained with the two particle streams sharing each half of the channel. At Window (1), particle trajectories were still unaffected by any magnetic forces. When moving to magnet front edge region, Window (2), similar magnetophoretic motions were observed for magnetic and diamagnetic particles as measured at 200 μL/hr. However, the buildup of magnetic particles was worse than what was found at 200 μL/hr as the amount of particles processed increased. At the magnet center of Window (3), the magnetophoretic phenomena for both magnetic and diamagnetic particles were still being developed at this flow rate and the tilted angles to the main flow direction were easy to read. Under such circumstances, the partial trapping for magnetic particles aggravated as more particles were entering the channel, hence more magnetic particles became trapped and held up a great amount of channel space that in turn helped enrich the local accumulation of ferrofluid nanoparticles, which restrained the escape of magnetic particle. When particle streams reached the junction area, Window (4), they each cover roughly half of the channel. In this sense, two types of particles were collected separately at different outlet reservoirs, enabling the particle separation using the both *positive* and *negative* magnetophoresis. It was determined that 230 μL/hr was the maximum flow rate for

particle streams to cover half without any overlapping. From 200 μL/hr, magnetic particles started to exit from the left branch when increasing the flow rate, gradually more magnetic particles could be collected from left branch with diamagnetic particle stream widening but limited to the right half. Consequently this separation utilizing both *positive* and *negative* magnetophoresis worked in a range from 200 μL/hr to 230 μL/hr.

Simulation results agreed with experimental ones for most cases, except that at 230 μL/hr, the two streams were not separated exactly at the microchannel centerline. This was again caused by the local aggregation of ferrofluid nano-particles at the magnet side that slightly diverted the flow towards the right side of the microchannel, therefore the separation point tended to move to the right side.

The experiment was run for more than 10 minutes, and a 2-minute video was taken at each outlet reservoir. Fig. 6-5 shows the superimposed images of these two reservoirs at consecutive time frames with a flow rate of 230 μL/hr, and it proves that this optimal separation can remain steady with impurities passing.

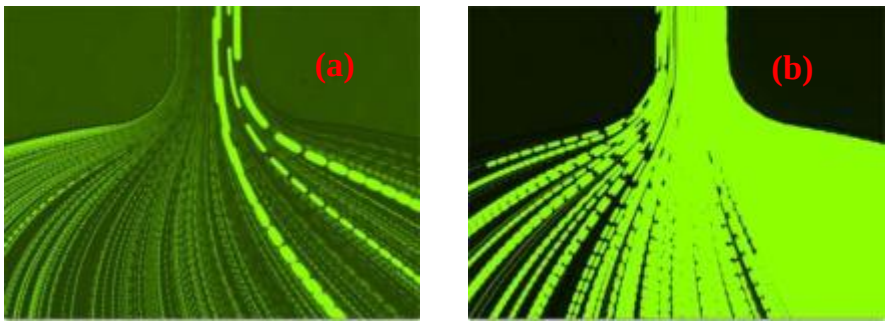

Fig. 6-5: Superimposed images for (a) left reservoir and (b) right reservoir at different time frames, flow rate is 230 μL/hr.

Further increasing the flow rate would cause overlapping of the two particle streams, since the deflection or attraction weakened as the flow rate increases, leaving one or both types of particles hard to retain its (or their) particle stream(s) in its (or their) own half. As in Fig 4(c), at 300 μL/hr, particles were less deflected or attracted at both magnet front edge and center regions, which suggested weaker magnetophoretic effects on these two particles. Meanwhile, at the magnet center region, less magnetic particles built as stronger flow flushed away the majority of the trapped particles. By the end of the straight section, Window (4), both particle streams were found covering more than half of the channel, therefore particles remained mixed at both outlet reservoirs and determined that the separation would fail at any flow rate larger than 230 μL/hr.

6.5. Conclusions

In this chapter, the magnetophoresis phenomenon was applied to achieve particle separation through the same T-shaped microchannel used earlier as a focusing device. The separation results from the deflections of two distinct magnetophoretic reactions of the particles towards individual directions of the flow. These deflections, predicted from the fundamental results, will grow with increasing particle size and decreasing flow rate. This holds true for both *positive* and *negative* magnetophoresis. Particularly, for this separation experiment, the flow rate needs to be carefully adjusted, since at certain small rates the trapping of magnetic particles will happen and continuous separation is unattainable.

Compared to the conventional MACS that either have to work in a batch mode or operate with low throughput for full trapping of magnetic particles has to be obtained, this second separation scheme made use of both *positive* and *negative* magnetophoresis by diverting two types of particles into different flow directions, and the trapping for magnetic particles was enhanced by the aggregation of ferrofluid nanoparticles. Therefore, this continuous separation method can work with a higher flow rate, thus increasing the throughput of the samples.

CHAPTER 7 : Conclusion and Future Work

This thesis investigated the particle motions in electrophoresis and magnetophoresis. These are two major aspects of microfluidic experiments, and extend from the fundamental observations and parametric studies to develop effective microfluidic devices that achieve particle focusing and particle separation with improvement from conventional methods. For each of the two methods, the particle motions were first studied using a simple rectangular straight microchannel. Based on the theoretical equations for the driving forces, the individual effect of every single key parameter was tested by holding other parameters fixed in values towards an optimized deflection rates. The observed variations of deflection rates according to these key parameters served a reliable foundation for the particle manipulation device design in the next step. Cooperated with the conventional manipulation methods in particle focusing and separation, this work fully explored the particle deflection in electrophoresis and magnetophoresis discovered earlier to establish new manipulation methods to resolve operation issues encountered in previous methods. More specifically, the conclusion and contribution of each chapter are summarized in the following text.

In Chapter 2, fundamental research of the particle electrophoresis in confined regions was performed, which showed a dielectrophoresis-resembled phenomenon on a particle while the particle flowed parallel to the microchannel wall. Both the experimental observation and simulated results confirmed that, the deflection rate increased with increasing particle size a and increasing electric field strength E. This electrophoretic deflection, different from conventional dielectrophoresis, can simply

works in a uniform microchannel without any changes in the geometry and it is envisioned that minor adjustments to the geometry will grant this device even more manipulation capabilities.

In Chapter 3, the electrophoretic deflection and related controlling effects were extended to both the microchannel width and depth directions. Initially randomly placed neutrally-buoyant particles were focused into a single file particle stream, exiting through the centerline of the microchannel. The same trend was detected for the focusing rates with respect to the particle size a and the electric field strength E. The obtained particle focusing can be recognized through optical detection, enabling an easy approach for cytometry applications. Additionally, the focusing in the depth direction prevents particle deposition and adhesion to bottom wall.

In Chapter 4, a fundamental experiment for particle magnetophoresis was conducted in a rectangular straight microchannel, demonstrating that under magnetic field gradients, particle deflection can be realized whenever differences exist in the magnetization capabilities between the particle and surrounding fluids. This magnetic approach enables a fast-processing and bio-compatible operation for clinical and other uses. Furthermore, an analytical model was developed to validate the particle deflection in ferrofluids. This 3D model was used to predict the critical flow rates for the particle focusing and separation in later experiments.

In Chapter 5, magnetophoresis was applied to establish a new particle focusing method. This method made use of the diamagnetic deflection and sheath flow in the side branch. This method only added a simple T-junction structure to the straight

microchannel, without any significant change to the fabrication complexity. Besides, the support of the sheath flow allowed this device to use only a single embedded magnet. Compared to a pair of repulsive magnets used in the conventional approach, the single magnet is easily embedded in the PDMS prior to the curing process of the fabrication. Moreover, with a single magnet, the magnet to microchannel distance is also conveniently adjustable without consideration of the minimum possible distance between repulsive magnets, which might cause distortion in the PDMS when the liquid PDMS is still soft during the cure.

In Chapter 6, the same T-shaped microchannel was used to achieve particle separation. The use of the same microchannel reflected a significant advantage of the microfluidic devices for being multi-functional. The separation was also based on the fundamental deflection, for both *positive* and *negative* magnetophoresis. The continuous working mode enables this separation device to surpass traditional MACS in both ease of operation and processing throughput.

To conclude, the electrokinetic methods are still the most well-studied microfluidic phenomenon, and also provide effective control of particles. The particle motions can be comprehensively explained by the developed theories. Therefore, the electrokinetic method will remain the mainstream manipulation method, while a future goal will be to design new microchannel systems that eventually reduce the energy input by utilizing the microchannel geometries and particle/medium properties. On the other hand, magnetic methods need to be fully studied regarding the ferrofluid nanoparticle and micro-particle/cell interactions, as these subtle phenomena may play an important role in

magnetic operations of the micro-scale magnetophoretic motion. Theoretical work has been published on magnetic behaviors and ferrofluid properties; hence, near future work is to develop a numerical model that integrates ferrofluid concentration variation response into a current flow and magnetic field solving model. Furthermore, the reliability and precision of the magnetic method also needs to be improved to provide robust performance. Interestingly, the study of combined electrokinetic and magnetic methods may provide a possible novel technology taking the advantages of both methods and with the two fields working together, Lorentz forces would emerge. As this force already directs the particle in the direction normal to both magnetic-induced and electrokinetic-driven directions, it can be envisioned that a three-dimensional operation can easily be realized using this combined method.

APPENDICES

Appendix A. Microchannel Fabrication

The channel geometry was designed in AutoCAD®, and printed onto a thin transparent film that later served as a negative photomask. Photoresist (SU-8 25, MicroChem Corp, Newton, MA) was dispensed onto a glass slide by spin-coating (WS-400E-NPP-Lite, Laurell Technologies, North Wales, PA), which yielded a uniform thickness of 25 μm. The slide was then subjected to a two-step soft bake at 65 ℃ and 95 ℃, respectively, to evaporate the solvent and densify the resist film. Following that, the resist was covered by the photomask for near UV light exposure (ABM Inc., San Jose, CA). After a two-step post-exposure bake at 65 ℃ and 95 ℃, the photoresist was developed in SU-8 developer forming the positive mold of the designed microchannel for PDMS casting.

The channel mold was put into a petri dish and covered with liquid PDMS (Dow Corning Corp., Midland, USA). After being degassed in an isotemp vacuum oven (13-262-280A, Fisher Scientific, Fair Lawn, NJ) for 30 minutes, the liquid PDMS was cured in a gravity convection oven (13-246-506GA, Fisher Scientific, Fair Lawn, NJ) at 70 ℃ for 2 hours. Once cured, the PDMS with the channel portion was cut out, and placed onto a clean glass slide with the channel side facing down. Two 5 mm-diameter through holes were then punched in the predesigned regions for reservoirs. Subsequently, the channel side of the PDMS slab was plasma-treated (PDC-32G, Harrick Scientific, Ossining, NY) along with another clean glass slide for 1 minute. Immediately following that, the two treated surfaces were bonded to form the microchannel.

Appendix B. Particle Visualization

Particle motion was visualized and recorded using an inverted microscope (Nikon Eclipse TE2000U, Nikon Instruments, Lewisville, TX) equipped with a CCD camera (Nikon DS-Qi1Mc). The obtained images were then processed using the Nikon imaging software (NIS-Elements AR 2.30).

REFERENCES

[1] Xuan, X., Zhu, J., Church, C., "Particle focusing in microfluidic devices", *Microfluidics and Nanofluidics*, 9 (2010) 1–16.

[2] Nilsson, J., Evander, M., Hammarstrom, B., Laurell, T., "Review of cell and particle trapping in microfluidic systems", *Analytica Chimica Acta*, 649 (2009) 141-157.

[3] Pamme, N., "Continuous flow separations in microfluidic devices", *Lab on a Chip*, 7 (2007) 1644–1659.

[4] Lenshof, A., Laurell, T., "Continuous separation of cells and particles in microfluidic systems", *Chemical Society Reviews*, 39 (2010) 1203-1217.

[5] Wong, P. K., Wang, T., Deval, J. H., Ho, C. M., "Electrokinetics in micro devices for biotechnology applications", *IEEE ASME Trans Mechatron*, 9 (2004) 366-376.

[6] Velev, O. D., Bhatt, K. H., "On-chip micromanipulation and assembly of colloidal particles by electric fields", *Soft Matter*, 2 (2006) 738-750.

[7] Laurell, T., Petersson, F., Nilsson, A., "Chip integrated strategies for acoustic separation and manipulation of cells and particles ", *Chemical Society Reviews*, 36 (2007) 492-506.

[8] Wang, Z., Zhe, J., "Recent advances in particle and droplet manipulation for lab-on-a-chip devices based on surface acoustic wave", *Lab on a Chip*, 7 (2011) 1280-1285.

[9] Pamme, N., "Magnetism and microfluidics", *Lab on a Chip*, 6 (2006) 24-38.

[10] Friedman, G., Yellen, B., "Magnetic Separation, Manipulation, and Assembly of Solid Phase in Fluids", *Current Opinion in Colloid and Interface Science.* 10 (2005) 158-166.

[11] Cho, S. H., Godin, J. M., Chen, C., Qiao, W., Lee, H., Lo, Y., "Review Article: Recent advancements in optofluidic flow cytometer", *Biomicrofluidics*, 4 (2010) 043001.

[12] Erickson, D., Serey, X., Chen, Y. F., Mandal, S., "Nanomanipulation using near field photonics", *Lab on a Chip*, 11 (2011) 995-1009.

[13] Gagnon, Z., Senapati, S., Gordon, J., Chang, H. C., "Dielectrophoretic detection and quantification of hybridized DNA molecules on nano-genetic particles", *Electrophoresis*, 29 (2008) 4808-12.

[14] Becker, F. F., Wang, X. B., Huang, Y., Pethig, R., Vykoukal, J., Gascoyne, P. R., "Separation of human breast cancer cells from blood by differential dielectric affinity", *Proceedings of the National Academy of Sciences*, 92 (1995) 860–864.

[15] Jang, L. S., Huang, P. H., Lan, K. C., "Single-cell trapping utilizing negative dielectrophoretic quadrupole and microwell electrodes", *Biosensors and Bioelectronics*, 24 (2009) 3637-44.

[16] Hunter, R. J., *Zeta potential in colloid science, principles and applications*, Academic Press, New York, 1981.

[17] Li, D., *Electrokinetics in Microfluidics*, Elsevier Academic Press, Burlington, 2004.

[18] Pohl, H. A., *Dielectrophoresis*, Cambridge University Press, Cambridge, 1978.

[19] Viovy, J., "Electrophoresis of DNA and other polyelectrolytes: physical mechanisms", *Reviews of Modern Physics*, 72 (2000) 813-872.

[20] Kang, Y., Li, D., "Electrokinetic motion of particles and cells in microchannels", *Microfluid. Nanofluid*, 6 (2009) 431-460.

[21] Anderson, J. L., "Colloid transport by interfacial forces", *Annual Review of Fluid Mechanics*, 21 (1989) 61-99.

[22] Keh, H. J., Anderson, J. L., "Boundary effects on electrophoretic motion of colloidal spheres", *Journal of Fluid Mechanics*, 153 (1985) 417-439.

[23] Keh, H. J., Lien, L. C., "Electrophoresis of a colloidal sphere along the axis of a circular orifice or a circular disk", *Journal of Fluid Mechanics*, 224 (1991) 305-333.

[24] Keh, H. J., Chiou, J. Y., "Electrophoresis of a colloidal sphere in a circular cylindrical pore", *AICHE Journal*, 42 (1996) 1397-1406.

[25] Shugai, A. A., Carnie, S. L., "Electrophoretic motion of a spherical particle with a thick double layer in bounded flows", *Journal of Colloid and Interface Science*, 213 (1999) 298-315.

[26] Ye, C., Sinton, D., Erickson, D., Li, D., "Electrophoretic motion of a cylindrical particle in a cylindrical microchannel", *Langmuir,* 18 (2002) 9095-9101.

[27] Xuan, X., B. Xu, D. Li, "Accelerated particle electrophoretic motion and separation in converging−diverging microchannels", *Analytical Chemistry*, 77 (2005) 4323-4328.

[28] Kang, K. H., Xuan, X., Kang, Y., Li, D., "Effects of dc-dielectrophoretic force on particle trajectories in microchannels", *Journal of Applied Physics*, 99 (2006) 064702.

[29] Qian, S. Z., Wang, A. H., Afonien, J. K., "Electrophoretic motion of a spherical particle in a converging–diverging nanotube", *Journal of Colloid Interface Science.* 303 (2006) 579-592.

[30] Yariv, E., Dorfman, K. D., "Electrophoretic transport through channels of periodically varying cross section", *Physics of Fluids*, 19 (2007) 037101.

[31] Ye, C., Li, D., "3-D transient electrophoretic motion of a spherical particle in a t-shaped rectangular microchannel", *Journal of Colloid Interface Science.* 272 (2004) 480-488.

[32] Davison, S. M., Sharp, K. V., "Transient simulations of the electrophoretic motion of a cylindrical particle through a 90 °corner", *Microfluidics and Nanofluidics.* 4 (2008) 409-418.

[33] Zhu, J., Tzeng, T. R., Hu, G., Xuan, X., "DC dielectrophoretic focusing of particles in a serpentine microchannel", *Microfluidics and Nanofluidics.* 7 (2009) 751-756.

[34] Zhu, J., Xuan, X., "Particle electrophoresis and dielectrophoresis in curved microchannels", *Journal of Colloid Interface Science.* 340 (2009) 285-290.

[35] Yariv, E., "“Force-free” electrophoresis?", *Physics of Fluids.* 18 (2006) 031702.

[36] Young, E., Li, D., "Dielectrophoretic force on a sphere near a planar boundary", *Langmuir.* 21 (2005) 12037-12046.

[37] Duffy, D. C., McDonald, J. C., Schueller, O. J. A., Whitesides, G. M., "Rapid prototyping of microfluidic systems in poly(dimethylsiloxane)", *Analytical Chemistry.* 70 (1998) 4974-4984.

[38] Xuan, X., Raghibizadeh, R., Li, D., "Wall effects on electrophoretic motion of spherical polystyrene particles in a rectangular poly(dimethylsiloxane) Microchannel", *Journal of Colloid Interface Science.* 296 (2006) 743-748.

[39] Keh, H. J., Chen, S. B., "Electrophoresis of a colloidal sphere parallel to a dielectric plane", *Journal of Fluid Mechanics* 194 (1988) 377-390.

[40] Yariv, E., Brenner, H., "The electrophoretic mobility of an eccentrically-positioned spherical particle in a cylindrical pore", *Physics of Fluids.* 14 (2002) 3354-3357.

[41] Happel, J., Brenner, H., *Low Reynolds Number Hydrodynamics*. Noordhoff International Publishing, Leyden, Netherlands, 1973.

[42] Israelachvili, J. N., *Intermolecular and Surface Forces*, Academic Press, San Diego, 1991.

[43] Xuan, X., "Joule heating in electrokinetic flow", *Electrophoresis*, 29 (2008) 33-43.

[44] Huh, D., Gu, W., Kamotani, Y., Grotgerg, J. B., Takayama, S., "Microfluidics for flow cytometric analysis of cells and particles", *Physiological Measurement*, 26 (2005) R73–R98.

[45] Chung, T. D., Kim, H. C., "Recent advances in miniaturized microfluidic flow cytometry for clinical use", *Electrophoresis*, 28 (2007) 4511–4520.

[46] Godin, J., Chen, C., Cho, S. H., Qiao, W., Tsai, F., Lo, Y. H., "Microfluidics and photonics for Bio-System-on-a-Chip: a review of advancements in technology towards a microfluidic flow cytometry chip", *Journal of Biophotonics*, 1 (2008) 355–376.

[47] Yu, C. H., Vykoukal, J., Vykoukal, D. M., Schwartz, J. A., Gascoyne, P. R. C., "A three-dimensional dielectrophoretic particle focusing channel for microcytometry applications", *Journal of Microelectromechanical Systems*, 14 (2005) 480–487.

[48] Chu, H., Doh, I., Cho, Y., "A three-dimensional (3D) particle focusing channel using the positive dielectrophoresis (pDEP) guided by a dielectric structure between two planar electrodes", *Lab on a Chip*, 9 (2009) 686–691.

[49] Voldman, J., "Electrical forces for microscale cell manipulation", *Annual Review of Biomedical Engineering*, 8 (2006) 425–454.

[50] Hawkins, B. G., Kirby, B. J., "Electrothermal flow effects in insulating (electrodeless) dielectrophoresis systems", *Electrophoresis*, 31 (2010) 3622–3633.

[51] Sridharan, S., Zhu, J., Hu, G., Xuan, X., "Joule heating effects on electroosmotic flow in insulator-based dielectrophoresis", *Electrophoresis*, 32 (2011) 2274–2281.

[52] Cheng, N., "Formula for viscosity of glycerol-water mixture", *Industrial and Engineering Chemistry Research*, 47 (2008) 3285-3288.

[53] Yang, Y., Zhang, H., Zhu, J., Wang, G., Tzeng, T., Xuan, X., Huang, K., Wang, P., "Distinguishing the viability of a single yeast cell with an ultra-sensitive radio frequency sensor", *Lab on a Chip*, 10 (2010) 553-555.

[54] Nicole, P., Andreas, M., "On-chip free-flow magnetophoresis: continuous-flow separation of magnetic particles and agglomerates", *Analytical Chemistry.* 76 (2004) 7250-7256.

[55] Rosensweig, R. E., "Fluidmagnetic buoyancy", *AIAA Journal*. 4 (1966) 1751–1758.

[56] Mirica, K. A., Shevkoplyas, S. S., Phillips, S. T., Gupta, M., Whitesides, G. M., "Measuring densities of solids and liquids using magnetic levitation: fundamentals", *Journal of the American Chemical Society.* 131 (2009) 10049–10058.

[57] Mark, D. T., Noriyuki, H., Alexander, I., Nicole, P., "On-chip diamagnetic repulsion in continuous flow", *Science and Technology of Advanced Materials.* 10 (2009) 014611.

[58] Angeles, I. R., Mark, D. T., Leigh, A. M., Julia, B. L., John, G., Josep, S., Nicole, P., "Flow focussing of particles and cells based on their intrinsic properties using a simple diamagnetic repulsion setup", *Lab on a Chip*, 11 (2011) 1240-1248.

[59] Winkleman, A., Gudiksen, K. L., Ryan, D., Whitesides, G. M., "A magnetic trap for living cells suspended in a paramagnetic buffer", *Applied Physics Letters.* 85 (2004) 2411-2413.

[60] Rosensweig, R. E., "Magnetic Fluids", *Annual Review of Fluid Mechanics.* 19 (1987) 437-463.

[61] Sharpe, S. A., *Magnetophoretic cell clarification*, MIT, PhD dissertation, 2004.

[62] Fateen, S. K., *Magnetophoretic focusing of submicron particles dispersed in a polymer-stabilized magnetic fluid*, MIT, PhD dissertation, 2002.

[63] Zhu, T., Lichlyter, D. J., Haidekker, M. A., Mao, L., "Analytical model of microfluidic transport of non-magnetic particles in ferrofluids under the influence of a permanent magnet", *Microfluidics and Nanofluidics.* 10 (2011) 1233-1245.

[64] Erb, R. M., Yellen, B., *Nanoscale Magnetic Materials and Applications*, J. P. Liu ed., 563-590, 2009.

[65] Rosensweig, R. E., *Ferrohydrodynamics*, Cambridge University Press, Cambridge, 1985.

[66] Furlani, E. P., *Permanent Magnet and Electromechanical Devices: Materials, Analysis, and Applications*, Academic Press, 2001.

[67] White, F. M., *Viscous Fluid Flow*, McGraw-Hill Science/Engineering/Math, 1991.

[68] Carlo, D. Di, Irimia, D., Tompkins, R. G., Toner, M., "Equilibrium separation and filtration of particles using differential inertial focusing", *Proceedings of the National Academy of Sciences.* 104 (2007) 18892-18897.

[69] Odenbach, S., *Magnetoviscous Effects in Ferrofluids*, Springer, 2002.

[70] Gijs, M. A. M., "Magnetic bead handling on-chip: new opportunities for analytical applications", *Microfluidics and Nanofluidics*, 1 (2004) 22–40.

[71] Gijs, M. A. M., Lacharme, F., Lehmann, U., "Microfluidic applications of magnetic particles for biological analysis and catalysis", *Chemical Reviews*, 110 (2010) 1518–1563.

[72] Nguyen, N. T., "Micro-magnetofluidics: interactions between magnetism and fluid flow on the microscale", *Microfluidics and Nanofluidics*, 12 (2012) 1–16.

[73] Afshar, R., Moser, Y., Lehnert, T., Gijs, M. A. M., "Three-dimensional magnetic focusing of superparamagnetic beads for on-chip agglutination assays", *Analytical Chemistry*, 83 (2011) 1022–1029.

[74] Peyman, S. A., Kwan, E. Y., Margarson, O., Iles, A., Pamme, N., "Diamagnetic repulsion--a versatile tool for label-free particle handling in microfluidic devices", *Journal of Chromatography A.* 1216 (2009) 9055-9062.

[75] Zhu, T., Cheng, R., Mao, L., "Focusing microparticles in a microfluidic channel with ferrofluids", *Microfluidics and Nanofluidics.* 11 (2011) 695-701.

[76] Rodriguez-Villarreal, A. I., Tarn, M. D., Madden, L. A., Lutz, J. B., Greenman, J., Samitier, J., Pamme, N., "Flow focusing of particles and cells based on their intrinsic properties using a simple diamagnetic repulsion setup", *Lab on a Chip*, 11 (2011) 1240–1248.

[77] Wen, C., Yeh, C., Tsai, C., Fu, L., "Rapid magnetic microfluidic mixer utilizing AC electromagnetic field", *Electrophoresis*, 30 (2009) 4179–4186.

[78] Pethig. R., "Review Article—Dielectrophoresis: Status of the theory, technology, and applications", *Biomicrofluidics*, 4 (2010) 022811.

[79] Cetin, B., Li, D., "Dielectrophoresis in microfluidics technology", *Electrophoresis*, 32 (2011) 2410.

[80] Lin, S., Mao, X., Huang, T., "Surface acoustic wave (SAW) acoustophoresis: now and beyond", *Lab on a Chip*, 12 (2012) 2766.

[81] Kayani, A. A., Khoshmanesh, K., Ward, S. A., Mitchell, A., Kalantar-zadeh, K., "Optofluidics incorporating actively controlled micro- and nano-particles", *Biomicrofluidics*, 6 (2012) 031501.

[82] Liu, C., Stakenborg, T., Peeters, S., Lagae, L., "Electron and photon spread contributions to the radiological penumbra for small monoenergetic x-ray beam (≤ 2 MeV)", *Journal of Applied Physics.* 105 (2009) 102011–102014.

[83] Miltenyi, S., Müller, W., Weichel, W., Radbruch, A., "High gradient magnetic cell separation with MACS", *Cytometry.* 11 (1990) 231-238.

[84] Kantor, A.B., Gibbons, I., Miltenyi, S., Schmitz, J., *Magnetic Cell Sorting with Colloidal Superparamagnetic Particles in Cell Separation Methods and Applications*, Marcel Dekker, New York, 1998.

[85] Choi, J., Ahn, C. H., Bhansali, S., Henderson, H. T., "A new magnetic bead-based, filterless bio-separator with planar electromagnet surfaces for integrated bio-detection systems", *Sensors and Actuators B*. 68 (2000) 34.

[86] Inglis, D., Riehn, R., Austin, R., and Sturm, J., "Microfluidic high gradient magnetic cell separation", *Applied Physics Letters.* 85 (2004) 5093-5095.

[87] Chalmers, J. J., Zborowski, M., Sun, L., Moore, L., "Flow through, immunomagnetic cell separation", *Biotechnology Progress*. 14 (1998) 141.

[88] Adams, J. D., Kim, U., Soh, H. T., "Multitarget magnetic activated cell sorter", *Proceedings of the National Academy of Sciences*. 105 (2008) 18165–18170.

[89] Adams, J. D., Thevoz, P., Bruus, H., Soh, H. T., "Integrated acoustic and magnetic separation in microfluidic channels", *Applied Physics Letters*. 95 (2009) 254103.

[90] Pamme, N., Wilhelm, C., "Continuous sorting of magnetic cells via on-chip free-flow magnetophoresis", *Lab on a Chip*, 6 (2006) 974-980.

[91] Zhu, T., Marrero, F., Mao, L., "Continuous separation of non-magnetic particles inside ferrofluids", *Microfluidics and Nanofluidics.* 9 (2010) 1003-1009.

[92] Furlani, E. P., "Analysis of particle transport in a magnetophoretic microsystem", *Journal of Applied Physics.* 99 (2006) 024912.

[93] Erb, R. M., Yellen, B. B., "Concentration gradients in mixed magnetic and nonmagnetic colloidal suspensions", *Journal Of Applied Physics*, 103 (2008) 07A312.

[94] Erb, R. M., Sebba, D. S., Lazarides, A. A., Yellen, B. B., "Magnetic field induced concentration gradients in magnetic nanoparticle suspensions: Theory and Experiment", *Journal of Applied Physics*, 103 (2008) 063916.